



# Assessment of the performance of large- capacity pumps used in waterways: experimental tests and computational modelling

UNIVERSITE DE LIEGE

OCTOBER 2021



**LIÈGE**  
université

# Table of contents

Table of contents.....	1
1 Introduction.....	2
2 Data and methods.....	2
2.1 Test bench.....	2
2.1.1 Tank and hydraulic set-up (piping) .....	2
2.1.2 Sensors, measurement devices.....	3
2.1.3 Test procedure .....	5
2.2 Computational model .....	7
2.2.1 Governing equations.....	7
2.2.2 Numerical resolution .....	14
2.2.3 Calibration procedure .....	19
2.2.4 Uncertainties estimation.....	22
2.2.5 Software implementation.....	23
2.2.6 Study examples .....	25
2.3 Tested pumps.....	27
2.3.1 Pump 1: Amarex KRTK 250 - 400/206UG-S.....	27
2.3.2 Pump 2: Flygt 3171.181 LT611.....	29
3 Results .....	32
3.1 Experimental observation.....	32
3.1.1 Pump 1: Amarex KRTK 250 - 400/206UG-S.....	32
3.1.2 Pump 2: Flygt 3171.181 LT611.....	33
3.2 Computational results.....	34
3.2.1 Pump1: Amarex KRTK 250 - 400/206UG-S.....	34
3.2.2 Pump 2: Flygt 3171.181 LT611.....	45
4 Conclusions.....	48
5 References.....	48
6 Appendices.....	50
6.1 Appendix 1: pump equations.....	50
6.2 Appendix 2: FLYGT datasheet .....	50

# 1 Introduction

A suitable tool to evaluate the actual on-site energy efficiency of pumping systems used in waterways is missing. Indeed, pump manufacturers generally provide detailed information on a curve of pump efficiency at nominal rotation speed. In contrast, no or little information is available concerning off-design pump operation for varying speed, while variable speed drives are known to enable increasing the overall efficiency of the pumping system, which is precisely what matters for the end-users. A hybrid modelling approach is presented here. It involves a large experimental test bench [4] used for calibrating a computational model of the whole system, including the motor, the pump and the hydraulic setting.

The following report details the testing of large-capacity pumps used in waterways based on a test bench built in the university of Liège. Section 2.1 details the test bench characteristics (the layout of piping, the sensors and the test procedure); a computational model of the pumping process; and the characteristics of the tested pumps. Experimental and computational results are presented in Section 2.3. Conclusion are drawn in Section 2.4.

## 2 Data and methods

### 2.1 Test bench

#### 2.1.1 Tank and hydraulic set-up (piping)

The overall objective of the test bench is to enable monitoring the efficiency of submersible and dry-action centrifugal pumps under a broad range of operating conditions. The primary goal being the assessment of pumps typically used for lifting water in artificial waterways, the capacity requirements for the test bench were defined in close collaboration with partners of the Green WIN project<sup>1</sup>. This lead to the following specifications: pressure up to 10 bars at the outlet of the tested pump, flow rate up to 0.3 m<sup>3</sup>/s, power supply up to 300 kW and pumps of up to 2 tons in weight (Table 1). Given these specifications, various aspects of the test bench were designed and sized: layout of stainless steel pipes, pipe diameters, water supply system, regulating valve, energy dissipation system, power electronic boxes with safety and emergency systems, pressure measurement devices and release of entrapped air, among others. A closed-loop system was selected. The overall layout is represented in the CAD model shown in Figure 1. The positioning of dry-action pumps to be tested is sketched on the right side of the figure, while submersible pumps to be tested shall be installed inside the large tank (visible on the left of the figure).

Tank characteristics		Pump characteristics		Test bench characteristics	
Weight	3.5 T	Weight max.	2 T	Sensors	10+
Capacity	30 m <sup>3</sup>	Power max.	300 kW	Area	8 m x 10 m
Diameter	3 m	Flow rate max.	300 l/s	Piping weight	2 T
Height	4.5 m	Pressure max.	10 bar	Height max	4.5 m

Table 1: Main characteristics of the test bench

The measurement system includes a flowmeter, a regulating valve (to adjust the head), pressure transducers as well as a power analyser and NI data logger. The main pipes have a diameter DN350, allowing friction losses to remain relatively low and ensuring that the diameter of the pump outlet is

<sup>1</sup> <https://www.nweurope.eu/projects/project-search/greenwin-greener-waterway-infrastructure/>

smaller than the pipe diameter. Sufficiently long straight pipe sections are placed at the inlet of the flowmeter as well as for the suction pipe of dry-action pumps, to ensure uniform velocity and pressure distribution on the considered section as this helps avoiding swirl conditions.

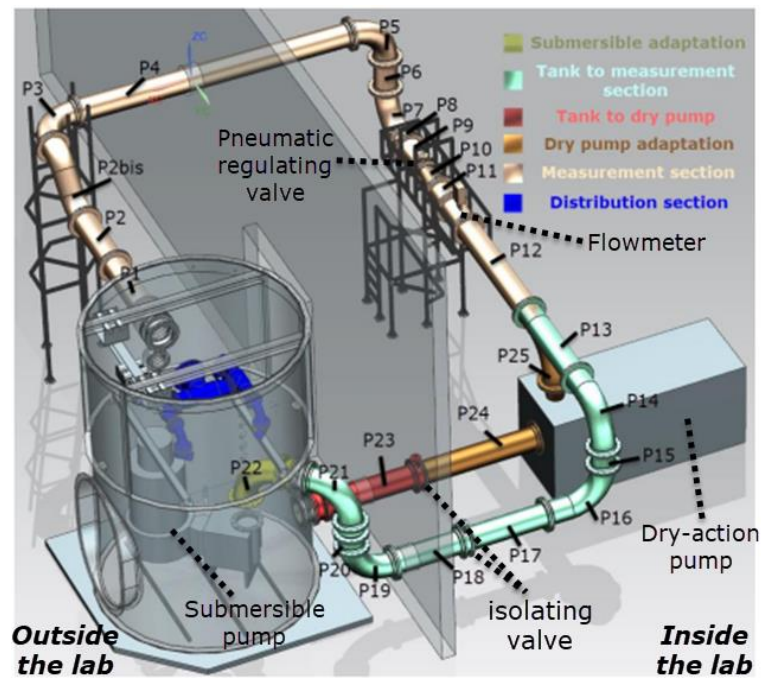


Figure 1: Layout of the test bench

The diameter and the height of the main tank were determined to prevent swirl conditions at the inlet of the submersible pumps [14]. Given the resulting dimensions (3 m in diameter and 4.5 m in height), the main tank was not available off-the-shelf; but it was manufactured on purpose for the construction of the test bench. It is made of stainless steel and its sizing accounts for a variety of constrains, including mechanical strength (finite element simulations were performed to size the curved door and lid), manufacturing process, pump installation procedure and test operations. The door is curved to withstand the inside pressure when the tank is filled with water. The stainless steel sheets are all minimum 6 mm thick. An energy dissipation system, made of several distribution pipes (in dark blue in Figure 1), is designed at the inlet of the tank to further contribute to avoiding swirl conditions close to the inlet of submersible pumps. A regulating valve is used to adjust the head losses in the hydraulic loop by varying the valve opening angle (between 30° and 70°). Given the specifications on the operation range of the pumps to be tested, a butterfly valve of diameter DN200 was selected.

### 2.1.2 Sensors, measurement devices

The test bench is equipped with several sensors. The main measuring devices are:

- An ISOIL electromagnetic flow meter MS2500+MV110 DN350, is located between pipes P11 and P12 (inside the lab). It measures a flow rate between 16.0 to 492 l/s with an accuracy of 0.4 %. At lower flow velocity, the accuracy decreases following the inverse of the flow velocity (Figure 2).

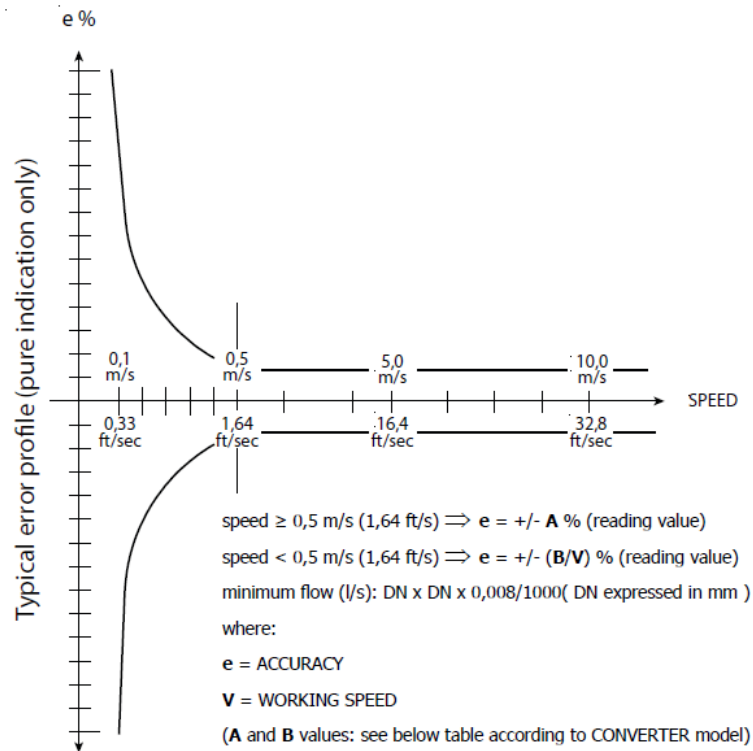


Figure 2: Flowmeter MS2500 with a MV110 converter: A=0.4 and B=0.4 m/s in [6]

- Two differential pressure transducers DP4000 are calibrated respectively to 0-10 bar and 0-0.4 bar inside the lab and are measuring the differential pressure between respectively the inlet and the outlet of the pump; and the inlet of the pump and the top of the tank in the air. Considering submersible pump, the pressure is taken at four points in the pipe P20 and in the immersed part of the tank (at its bottom) to record the pump head. The other pressure transducer measures the pressure difference between the emerged part of the tank and the pump inlet (i.e the tank). This last one has as goal to measure the water level inside the tank. Considering dry-action pump, the pump head is measured by pressure difference between a four points measurement located in pipe P24 and one located in pipe P25. The other transducer measures the difference between pipe P24 and the emerged part of the tank. The two sensors are working with an accuracy of 0.075 %.
- A multifunctional power monitor Sineax-AM2000 and current transformers 1/5 measures the active power provided to a variable frequency drive connected to the pump. Its accuracy is about 0.5%.

All quantities measured with the main sensors are noted in Table 2 with their corresponding accuracy.

NOTATION	UNITS	Physical meaning	Accuracy	Device
$\tilde{Q}^*$	m <sup>3</sup> /s	Measured flow rate	0.4%	MS2500
$\tilde{H}_p^*$	m	Measured pump Head	0.075%	DP4000
$\tilde{P}_e^*$	W	Measured electrical Power	0.5	Sineax-AM2000
$\tilde{\eta}_{tot}^*$	-	The total efficiency is indirectly measured by the formula: $\tilde{\eta}_{tot}^* = \frac{\rho g \tilde{H}_p^* \tilde{Q}^*}{\tilde{P}_e^*}$	0.975%	

Table 2: Main measured quantities in the test bench

There is still additional equipment such as:

- Two vibrating fork level switch to detect when the tank is filled and when it is empty. One is installed at the bottom of the tank and the other one at the top.
- Thermocouples are installed to verify that the water temperature does not change too much.

### 2.1.3 Test procedure

A test procedure is established to draw characteristic curves of the pump with associated performance for nominal and off-design operation. To this aim, both head losses and the rotation speed is tuned. Two procedures were used to test pumps. The procedure is as follow:

1. **Install pump:** Submersible pumps to be tested are placed inside the tank through the door using a fork truck lift machine and the bridge crane installed at the top of the tank while dry-action pumps are placed inside laboratory;
2. **Fill the tank:** the tank is filled using laboratory pump through DN100 pipes;
3. **Bleed air in the pipes:** the pump test bench is bled everywhere in the bench where air is entrapped, i.e in P11, P21 and P3. A vacuum device using Venturi principle is used to vacuum the pipe P3 since this one is above the free surface inside the tank;
4. **Start a testing procedure:** to draw characteristic curve of the tested pump, two variables need to be systematically varied: the head losses and the rotation speed (via the frequency applied on the pump motor). A valve is used to generate the desired head losses and a variable frequency drive is used to control the rotation speed. The procedure n°1 and n°2 differs from the way they achieve these two actions. The pump is started smoothly at a quite low rotation speed, with the lowest opening angle of the valve. It corresponds to state [0] in Figure 3. While the variables in the bench are continuously measured at a high frequency, the opening angle is increased by a step of  $\Delta A$ , up to the maximum flow rate of the pump or the valve maximum opening angle is reached, state [1] in Figure 3. Then, the operation is repeated in reversed order, by decreasing the valve opening angle to check previous measurements, state [2] in Figure 3. This step is only performed during the procedure n°2. Next, the pump rotating speed is increased by increasing the frequency by a predefined step  $\Delta f$ , state [3] in Figure 3 and the whole operation is repeated again until the maximum frequency is applied. Then, the pump is stopped, state [4] in Figure 3. The valve is fully open and the pump can be changed.

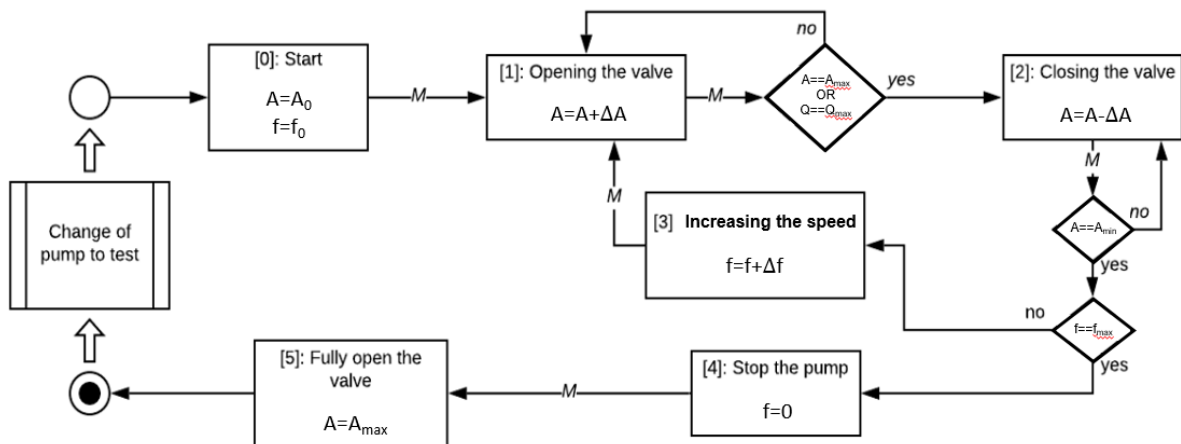


Figure 3: Block diagram of the testing procedure with five states using the following notations:  $A$  (the opening angle of the regulating valve; and  $\Delta A$ , the increment of opening angle);  $f$  (the frequency; and  $\Delta f$ , the increment of frequency);  $Q$  (the measured flow rate); and  $M$  (a Boolean value continuously checked, which is set to true if the measurements are steady during a time  $\Delta t$ ).

### Procedure n°1:

This procedure was used when the data acquisition was not already built. So, the variables are manually controlled and the measurements were performed by sight-reading on sensor screens. The pneumatic regulating valve was not yet controllable. Hence, the valve V1 in Figure 4, was used to vary the head losses via a hand-wheel. The frequency was manually set on the ABB frequency drive (provided by the thermodynamic lab).

During the tests, the water level was at 3.47 m with a suction inlet 2.97 m under the water free surface. The second differential pressure transmitter measures the useful head, i.e the difference of pressure between the bottom of the tank (Pr1, Figure 4) and a four point measurement at the pipe P20 (Pr2, Figure 4). The procedure is described in Figure 3 with a variable opening angle  $\Delta A$  (manually set to observe new operating point) and a variable frequency increment  $\Delta f$  (to run through the frequencies: 15, 25, 35, 45, 50 Hz).

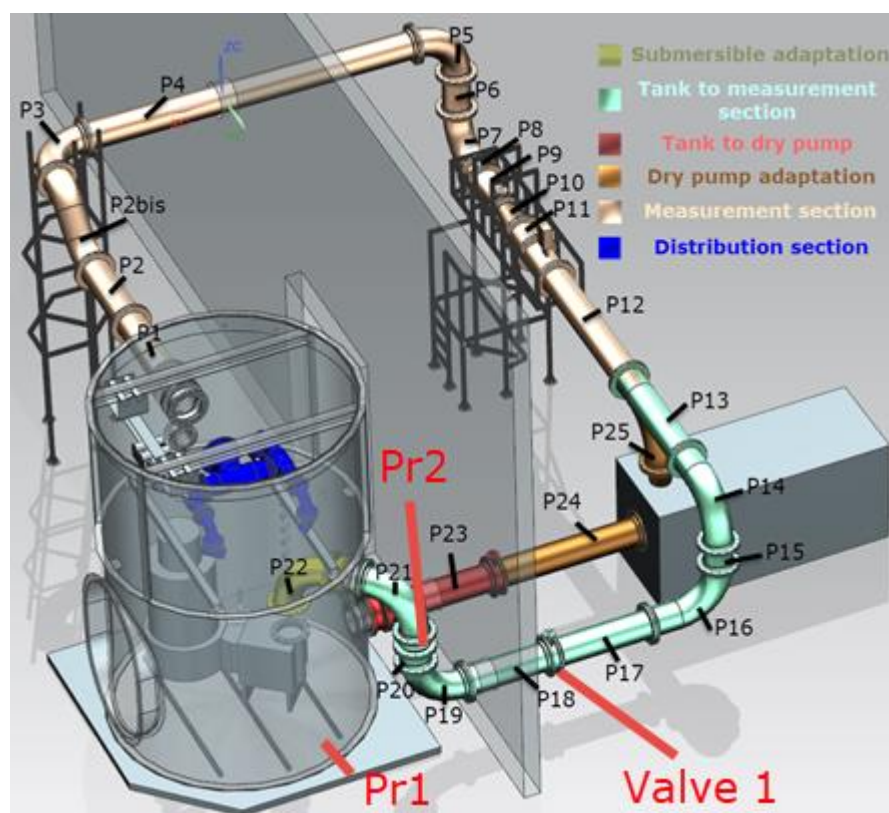


Figure 4 : CAD model of the pump test bench

### Procedure n°2:

This procedure has as goal to automate the test of a pump in the bench. It is currently in a writing phase, now that all the acquisition system is available to record measurements. The frequency increment  $\Delta f$  is fixed to a constant, 5 Hz (starting at 15Hz) and the opening angle increment  $\Delta A$  of the regulating valve with a constant increment of 10% (starting at 10%). The regulating valve and the rotation speed of the pump are electronically steered to browse a range of operating points, with a 4-20 mA signals for each one.

Procedure parameter	Value
$A_0$	10%
$f_0$	15 Hz
$\Delta A$	10%

$\Delta f$	5 Hz
$A_{max}$	100%
$A_{min}$	10%
$Q_{max}$	Not tested
$f_{max}$	50 Hz

Table 3: Procedure parameter applied to test pump

## 2.2 Computational model

### 2.2.1 Governing equations

The numerical model consists to define the operation of an assembly motor/pump as a steady-state system. The model simulates, in steady-state, the motor operation (assuming an induction motor), the pump wheel operation and the head losses in suction and discharge pipes. The model inputs are the frequency  $\omega_s$ , the voltage  $e_x$  applied to the windings of the motor (as a function of the connection type: either star [220 V] or delta [400 V] with a three-phase voltage of 400 V between phases) and the hydraulic configuration i.e, the head difference  $H_e$  and the head loss coefficient  $c_f$ . The model computes the operation point of the pump: currents  $I$ , magnetic fluxes  $\psi$ , voltage  $V$ , ... and particularly the flow rate  $Q$  and the head  $H$ . Some efficiencies can be deduced: pump  $\eta_p$ , motor  $\eta_m$ , hydraulic efficiency  $\eta_h$  and the overall efficiency  $\eta_{tot}$ .

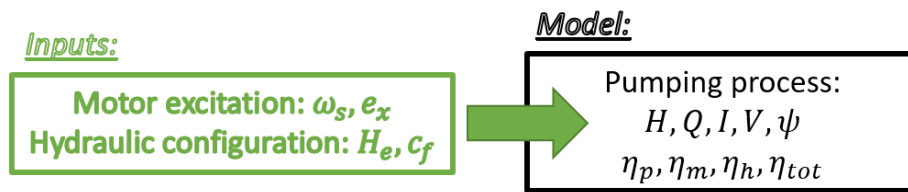


Figure 5 : Box of the numerical tool developed that computes the operating point of the pump (currents  $I$ , magnetic fluxes  $\psi$ , voltage  $V$ , ... and particularly the flow rate  $Q$ , the head  $H$  and the efficiencies of pump  $\eta_p$ , motor  $\eta_m$ , hydraulic efficiency  $\eta_h$  and overall efficiency  $\eta_{tot}$ ) based on controlled inputs (the frequency  $\omega_s$ , the voltage  $e_x$  and the hydraulic configuration i.e, the head difference  $H_e$  and a coefficient of head losses  $c_f$ ).

To make the model formulation dimensionless, a number of characteristic quantities also called base values are defined, as detailed in Table 4. All variables are divided by their corresponding base value (subscript  $\square_B$ ) to formulate dimensionless equations.

Units	Basis
Time [s]	$t_B = \frac{1}{\omega_B} = \frac{1}{2\pi f_B}$
Power [VA]	$S_B = \frac{P_n}{PF}$
Voltage [V]	$V_B$
Current [A]	$I_B = \frac{S_B}{3V_B}$
Impedance [ $\Omega$ ]	$Z_B = \frac{3V_B^2}{S_B}$
Flux [Wb]	$\psi_B = V_B t_B$
Rotor speed [ $s^{-1}$ ]	$\omega_{mB} = \frac{\omega_B}{p}$
Torque [Nm]	$T_B = \frac{S_B}{\omega_{mB}}$
Head [m]	$H_B = H_p(Q = 0)$
Flow rate [ $m^3/s$ ]	$Q_B = \frac{S_B}{\rho g H_B}$

Table 4 : Per unit system used for the asynchronous motor driving the pump where  $f_B$  stands for the nominal frequency,  $P_n$  the nominal electric power,  $PF$  the power factor,  $V_B$  the nominal voltage,  $H_p(Q = 0)$  the pump head for a zero flow rate and  $p$  the number of pair of poles.

The dimensionless equations constituting the model are:

$$v_{ds} = e_y - R_e i_{ds} - \omega_s L_e i_{qs} \quad (1)$$

$$v_{qs} = e_x - R_e i_{qs} + \omega_s L_e i_{ds} \quad (2)$$

$$v_{ds} = R_s i_{ds} + \omega_s \psi_{qs} \quad (3)$$

$$v_{qs} = R_s i_{qs} - \omega_s \psi_{ds} \quad (4)$$

$$0 = R_r i_{dr} + (\omega_s - \omega_r) \psi_{qr} \quad (5)$$

$$0 = R_r i_{qr} - (\omega_s - \omega_r) \psi_{dr} \quad (6)$$

$$\psi_{ds} = L_{ss} i_{ds} + L_{sr} i_{dr} \quad (7)$$

$$\psi_{qs} = L_{ss} i_{qs} + L_{sr} i_{qr} \quad (8)$$

$$\psi_{dr} = L_{sr} i_{ds} + L_{rr} i_{dr} \quad (9)$$

$$\psi_{qr} = L_{sr} i_{qs} + L_{rr} i_{qr} \quad (10)$$

$$0 = (\psi_{dr} i_{qr} - \psi_{qr} i_{dr}) - (A_{fr} \omega_r + B_{fr} \omega_r^2) - (dQ^2 + eQ \omega_r + f_* \omega_r^2) \quad (11)$$

$$H_p = aQ^2 + bQ \omega_r + c\omega_r^2 \quad (12)$$

$$H_p = H_e + c_f Q^2 \quad (13)$$

where the subscripts  $d$ ,  $q$ ,  $s$  and  $r$  relate to the  $d$  axis of the Park transformation [2], the  $q$  axis of the Park transformation [2], the stator and the rotor. The 10 first equations models the behaviour of an induction motor explained in [10]. The parameters of the model are listed in Table 5. Their values are specific to each pump and should be identified experimentally. The standard ranges of variations of their dimensionless form are given in Table 6. The input data of the numerical model are detailed in Table 7. The resolution of the 13 equations allows computing the 13 unknowns listed in Table 8.

Dimensional quantities		Dimensionless quantities	Physical meaning
NOTATION	UNITS		
$\tilde{R}_e$	$\Omega$	$R_e = \tilde{R}_e / Z_B \geq 0$	Resistance of the motor power cable
$\tilde{L}_e$	H	$L_e = \tilde{L}_e / (Z_B t_B) \geq 0$	Inductance of the motor power cable
$\tilde{R}_s$	$\Omega$	$R_s = \tilde{R}_s / Z_B \geq 0$	Stator winding resistance
$\tilde{R}_r$	$\Omega$	$R_r = \tilde{R}_r / Z_B \geq 0$	Rotor winding resistance
$\tilde{L}_{ss}$	H	$L_{ss} = \tilde{L}_{ss} / (Z_B t_B) \geq 0$	Equivalent inductance of the stator

$\tilde{L}_{sr}$	H	$L_{sr} = \tilde{L}_{sr}/(Z_B t_B) \geq 0$	Equivalent mutual inductance
$\tilde{L}_{rr}$	H	$L_{rr} = \tilde{L}_{rr}/(Z_B t_B) \geq 0$	Equivalent inductance of the rotor
$\tilde{A}_{fr}$	Nm s	$A_{fr} = \frac{\tilde{A}_{fr} \omega_{mB}}{T_B} \geq 0$	Coefficient modelling the viscous friction inside the motor
$\tilde{B}_{fr}$	Nm s <sup>2</sup>	$B_{fr} = \frac{\tilde{B}_{fr} \omega_{mB}^2}{T_B} \geq 0$	Coefficient modelling the friction inside the motor between rotor and air; and between the inner ring of the ball bearing and oil.
$\tilde{a}$	m <sup>-5</sup> s <sup>2</sup>	$a = \tilde{a} Q_B^2 / H_B$	Coefficients used to compute the pump head as a parabolic function of the flow rate
$\tilde{b}$	m <sup>-2</sup> s <sup>2</sup>	$b = \tilde{b} Q_B \omega_{mB} / H_B$	
$\tilde{c}$	m s <sup>2</sup>	$c = \tilde{c} \omega_{mB}^2 / H_B \geq 0$	
$\tilde{d}$	Nm <sup>-5</sup> s <sup>2</sup>	$d = \tilde{d} Q_B^2 / T_B$	Coefficients used to compute the pump torque as a parabolic function of the rotation speed
$\tilde{e}$	Nm <sup>-2</sup> s <sup>2</sup>	$e = \tilde{e} Q_B \omega_{mB} / T_B$	
$\tilde{f}_*$	Nm s <sup>2</sup>	$f_* = \tilde{f}_* \omega_{mB}^2 / T_B \geq 0$	

Table 5: Parameter of the pump numerical model

$R_s$	0.01 – 0.12	$R_r$	0.01 – 0.13
$L_{ss} - L_{sr}$	0.07 – 0.15	$L_{rr} - L_{sr}$	0.06 – 0.18
$L_{sr}$	1.8 – 3.8		

Table 6: Range of dimensionless parameter on the machine base

Dimensional quantities		Dimensionless quantities	Physical meaning
NOTATION	UNITS		
$\tilde{\omega}_s$	Hz	$\omega_s = \tilde{\omega}_s / f_B \geq 0$	Frequency applied to the motor
$\tilde{e}_x$	V	$0 \leq e_x = \tilde{e}_x / (V_B) \leq 1$	Voltage applied to the motor
$\tilde{c}_f$	m <sup>-5</sup> s <sup>2</sup>	$c_f = \frac{\tilde{c}_f Q_B^2}{H_B} \geq 0$	It is a coefficient to compute the total head losses and is given by the sum of all head losses coefficient $k$ in suction and discharge pipes: $\tilde{c}_f = \sum_i \frac{k_i}{g A_i^2}$ with $k_i$ , the head losses coefficient of the $i^{\text{th}}$ part of the pipes; $g$ (9.81 m/s <sup>2</sup> ) and $A_i$ , the section of the $i^{\text{th}}$ part of the pipes.
$\tilde{H}_e$	m	$H_e = \tilde{H}_e / H_B \geq 0$	The head difference between navigation reach

Table 7: Inputs of the pump numerical model

Dimensional quantities		Dimensionless quantities	Physical meaning
NOTATION	UNITS		
$\tilde{i}_{ds}$	A	$i_{ds} = \frac{\tilde{i}_{ds}}{\sqrt{3} I_B}$	Current in the stator fictive Park winding 'd'
$\tilde{i}_{qs}$	A	$i_{qs} = \frac{\tilde{i}_{qs}}{\sqrt{3} I_B}$	Current in the stator fictive Park winding 'q'
$\tilde{i}_{dr}$	A	$i_{dr} = \frac{\tilde{i}_{dr}}{\sqrt{3} I_B}$	Current in the rotor fictive Park winding 'd'
$\tilde{i}_{qr}$	A	$i_{qr} = \frac{\tilde{i}_{qr}}{\sqrt{3} I_B}$	Current in the rotor fictive Park winding 'q'
$\tilde{v}_{ds}$	V	$v_{ds} = \frac{\tilde{v}_{ds}}{\sqrt{3} V_B}$	Tension in the stator fictive Park winding 'd'

$\tilde{v}_{qs}$	V	$v_{qs} = \frac{\tilde{v}_{qs}}{\sqrt{3}V_B}$	Tension in the stator fictive Park winding 'q'
$\tilde{\psi}_{ds}$	Wb	$\psi_{ds} = \frac{\tilde{\psi}_{ds}}{\sqrt{3}\psi_B}$	Magnetic flux entering in the stator fictive Park winding 'd'
$\tilde{\psi}_{qs}$	Wb	$\psi_{qs} = \frac{\tilde{\psi}_{qs}}{\sqrt{3}\psi_B}$	Magnetic flux entering in the stator fictive Park winding 'q'
$\tilde{\psi}_{dr}$	Wb	$\psi_{dr} = \frac{\tilde{\psi}_{dr}}{\sqrt{3}\psi_B}$	Magnetic flux entering in the rotor fictive Park winding 'd'
$\tilde{\psi}_{qr}$	Wb	$\psi_{qr} = \frac{\tilde{\psi}_{qr}}{\sqrt{3}\psi_B}$	Magnetic flux entering in the rotor fictive Park winding 'q'
$\tilde{\omega}_r$	rad/s	$\omega_r = \tilde{\omega}_r/\omega_{mB}$	Rotational speed of the rotor (same as pump)
$\tilde{Q}$	m <sup>3</sup> /s	$Q = \tilde{Q}/Q_B \geq 0$	Flow rate supplied by the pump
$\tilde{H}_p$	m	$H_p = \tilde{H}_p/H_B \geq 0$	Pump head

Table 8: Unknowns of the pump numerical model

The model has a degree of freedom due to the Park transformation. It is why, in the implementation,  $e_y$  is imposed to zero. Hence, the input voltage can be simplified and expressed as:

$$\sqrt{e_x^2 + e_y^2} = e_x$$

The losses and the inductance in the feeding cable are generally negligible:  $R_e = L_e = 0$ . Besides, if they were not negligible, increasing the coefficients  $R_s \leftarrow (R_s + R_e)$  and  $L_{ss} \leftarrow (L_{ss} + L_e)$  will lead to same operation since equations (1) and (3), as well as (2) and (4), can be merged respectively in:

$$e_y = (R_s + R_e)i_{ds} + \omega_s((L_{ss} + L_e)i_{qs} + L_{sr}i_{qr}) \quad (14)$$

$$e_x = (R_s + R_e)i_{qs} - \omega_s((L_{ss} + L_e)i_{ds} + L_{sr}i_{dr}) \quad (15)$$

Equation (11) expresses a torque balance where the electric torque  $T_e$ , a motor friction torque  $T_{fr}$  and the pump torque  $T_p$  are given by:

$$T_e = \psi_{dr}i_{qr} - \psi_{qr}i_{dr} \quad (16)$$

$$T_{fr} = A_{fr}\omega_r + B_{fr}\omega_r^2 \quad (17)$$

$$T_p = dQ^2 + eQ\omega_r + f_*\omega_r^2 \quad (18)$$

This second torque models a viscous friction [3] as can appear in ball bearing fitted with friction seals, and the drag in air and in bearing lubrication proportional to the square of the velocity [9]. For simplicity, static friction is not considered. The pump head curve is assumed to follow a quadratic expression of the flow rate [7] and the pump torque can be expressed here as a second degree polynomial of the rotation speed [18], [1]. The derivation of the pump torque and head equations may be obtained using the affinity laws [13] and a torque expression introduced by [11]. The details are explained in the appendix 6.1.

Several efficiencies can be evaluated once the numerical model is solved:

$$\eta_m = \frac{T_p\omega_r}{e_x i_{qs}} \quad (19)$$

$$\eta_p = \frac{H_p Q}{T_p\omega_r} \quad (20)$$

$$\eta_h = \frac{H_e}{H_p} \quad (21)$$

$$\eta_{tot} = \eta_m\eta_p\eta_h \quad (22)$$

The motor efficiency  $\eta_m$  (19) is the ratio between its power consumption and the mechanical power given to the pump wheel. The pump efficiency  $\eta_p$  (20) is defined as the hydraulic power generated over the mechanical power provided by the motor. The hydraulic efficiency  $\eta_h$  (21) is the ratio between the targeted head difference  $H_e$  and the total head difference which includes head losses and is equal to the pump head  $H_p$ . The overall efficiency  $\eta_{tot}$  (22) is the sum of these three parts.

If the pump is operating with a variable speed drive, one more relation should be taken into account: the control strategy. This one relates the power supply to the frequency applied. Thereby, one famous strategy is the scalar control. It consists to maintain a constant maximum electric torque such as displayed in Figure 6. The electric torque can be expressed by solving the equations (1) to (10) depending on the rotation speed  $\omega_r$ , the voltage  $e_x$  and the frequency  $\omega_s$ :

$$N_{Te} = L_{sr}^2 R_r (e_x^2 + e_y^2) \quad (23)$$

$$A_{Te} = \omega_s^2 (L_{rr} (L_{ss} + L_e) - L_{sr}^2) + L_{rr}^2 (R_e + R_s)^2 \quad (24)$$

$$B_{Te} = 2L_{sr}^2 R_r (R_s + R_e) \quad (25)$$

$$C_{Te} = R_r^2 ((R_e + R_s)^2 + \omega_s^2 (L_e + L_{ss})^2) \quad (26)$$

$$T_e(\omega_r, \omega_s, e_x) = \frac{N_{Te}(\omega_s - \omega_r)}{(\omega_s - \omega_r)(A_{Te}(\omega_s - \omega_r) + B_{Te}\omega_s) + C_{Te}} \quad (27)$$

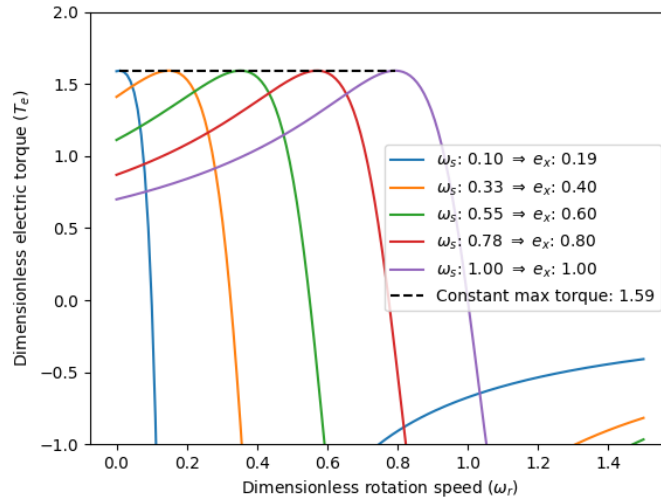


Figure 6: Electric torque curve for several excitation ( $\omega_s$ ;  $e_x$ ) and as example, value of parameters: [ $R_e$ : 0;  $L_e$ : 0;  $R_s$ : 0.05;  $R_r$ : 0.05;  $L_{sr}$ : 2;  $L_{ss}$ : 2.09;  $L_{rr}$ : 2.15].

The operating point of the induction motor is located between the maximum and the zero (corresponding to  $\omega_r = \omega_s$ ) on the electric torque curve and is defined as the intersection between the electric torque and the sum of friction and pump torque. The maximum torque and the corresponding rotation speed can be derived analytically:

$$T_{e,max} = \frac{N_{Te}}{2\sqrt{A_{Te}C_{Te} + B_{Te}\omega_s}} \quad (28)$$

$$\omega_{r,Tmax} = \omega_s - \sqrt{C_{Te}/A_{Te}} \quad (29)$$

Based on the principle of the scalar control, the maximum torque should be constant. Assuming stator resistance  $R_s$  is equal to zero, (28) is directly proportional to the square of  $e_x/\omega_s$ . Thereby, to maintain a constant maximum torque, the ratio  $e_x/\omega_s$  should be constant as told in [19]. But in practice, the rotor resistance is not equal to zero and a constant ratio  $e_x/\omega_s$  does not lead to a constant maximum torque. As seen in Figure 7, for low frequency, the voltage should be greater compared to the constant  $e_x/\omega_s$  strategy, in order to keep constant the maximum torque.

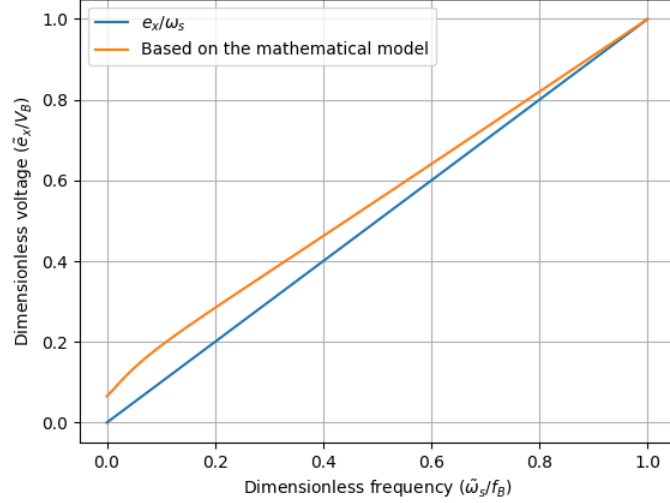


Figure 7: Control strategy to apply a scalar control: blue curve stands for a constant ratio  $e_x/\omega_s$  which is valid for stator resistance equals to zero; orange curve stands for the relationship needed between the voltage and frequency to maintain exactly the maximum torque constant.

Due to its simplicity, the constant ratio is still performed in VFD. Sometimes, the scalar control curve ( $\omega_s - e_x$ ) has an overshoot at low frequency to ensure a larger starting torque. Indeed, the maximum electric torque decreases for low frequency when a constant ratio  $e_x/\omega_s$  is applied as seen in Figure 8 and the torque may not be sufficient to start the motor.

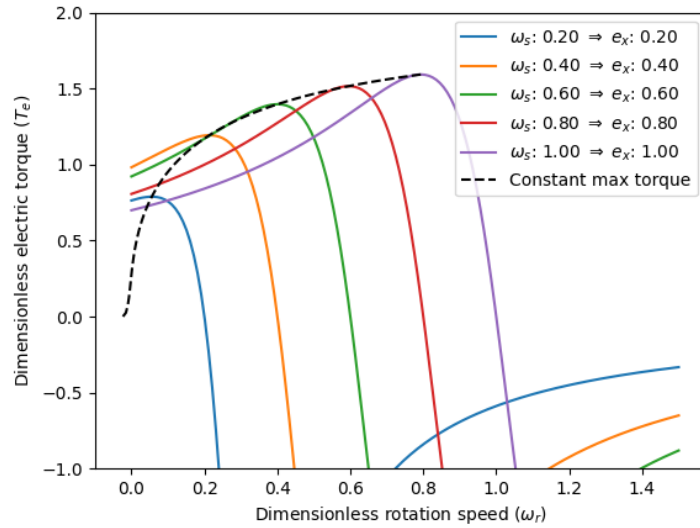


Figure 8: Electric torque curves when a constant ratio  $e_x/\omega_s$  strategy is applied with a non-zero rotor resistance

To avoid that cons, some VFD has the opportunity to control a bit the scalar strategy by implementing a kind of overshoot of voltage at the starting before to retrieve a constant ratio strategy as displayed in Figure 9 and Figure 10. It is corroborated by [12]. The relationship between voltage and frequency is given by:

$$c_{scalar} = \sqrt{(2T_{e,max}L_{rr}) (R_e + R_s)/L_{sr}} \quad (30)$$

$$\begin{cases} e_x = c_{scalar} + \frac{\omega_s}{\omega_{s,overshoot}} (\omega_{s,overshoot} - c_{scalar}) & \text{If } \omega_s \leq \omega_{s,overshoot} \\ e_x = \omega_s & \text{otherwise} \end{cases} \quad (31)$$

$$(32)$$

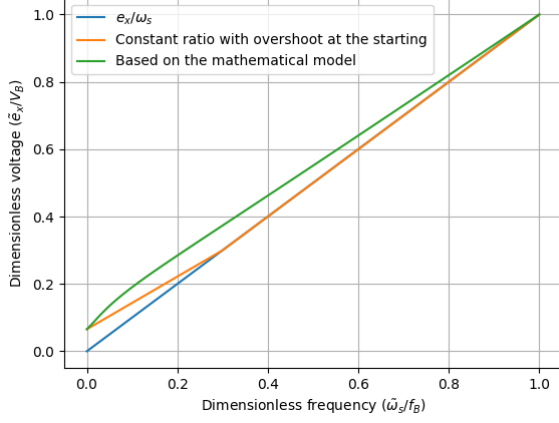


Figure 9: Constant ratio with an overshoot at the starting:  
 $\omega_{s,overshoot} = 0.3$

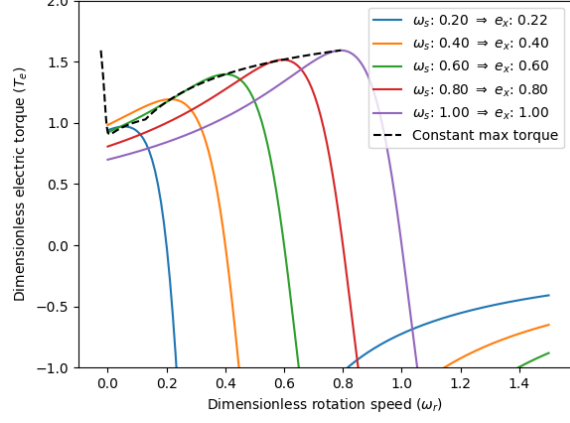


Figure 10: Electric torque curves applying a constant ratio strategy with a starting overshoot ( $\omega_{s,overshoot} = 0.3$ )

Finally, three kinds of scalar strategy may be used: the constant ratio  $e_x/\omega_s$ , the constant ratio with an overshoot for frequency below  $\omega_{s,overshoot}$ , and the exact relationship based on the mathematical model.

The global governing equations from (1) to (13) can be reduced to three equations with the unknowns  $\omega_r$ ,  $Q$  and  $H_p$ :

$$0 = T_e(\omega_r, \omega_s, e_x) - (A_{fr}\omega_r + B_{fr}\omega_r^2) - (dQ^2 + eQ\omega_r + f_*\omega_r^2) \quad (33)$$

$$H_p = aQ^2 + bQ\omega_r + c\omega_r^2 \quad (34)$$

$$H_p = H_e + c_f Q^2 \quad (35)$$

These three equations are very useful to understand the behaviour of the pump and to set appropriate guesses to resolve the non-linear system. This is detailed in the next section. Yet, to obtain the 10 first unknowns which relate to an electrical aspect, the 10 first equations [(1) to (10)] could be summarized to an AC circuit with phasors. The phasors introduced are: (with  $j$  the imaginary number)

$$\bar{E} = e_x + j e_y \quad (36)$$

$$\bar{V}_s = v_{qs} + j v_{ds} \quad (37)$$

$$\bar{I}_s = i_{qs} + j i_{ds} \quad (38)$$

$$\bar{I}_r = i_{qr} + j i_{dr} \quad (39)$$

$$\bar{\psi}_s = \psi_{qs} + j \psi_{ds} \quad (40)$$

$$\bar{\psi}_r = \psi_{qr} + j \psi_{dr} \quad (41)$$

The 10 first equations could be rewritten into five phasors equations:

$$\bar{E} = R_e \bar{I}_s + j \omega_s L_e \bar{I}_s \quad (42)$$

$$\bar{V}_s = R_s \bar{I}_s + j \omega_s (L_{ss} \bar{I}_s + L_{sr} \bar{I}_r) \quad (43)$$

$$0 = \frac{\omega_s}{\omega_s - \omega_r} R_r \bar{I}_r + j \omega_s (L_{sr} \bar{I}_s + L_{rr} \bar{I}_r) \quad (44)$$

$$\bar{\psi}_s = L_{ss} \bar{I}_s + L_{sr} \bar{I}_r \quad (45)$$

$$\bar{\psi}_r = L_{sr} \bar{I}_s + L_{rr} \bar{I}_r \quad (46)$$

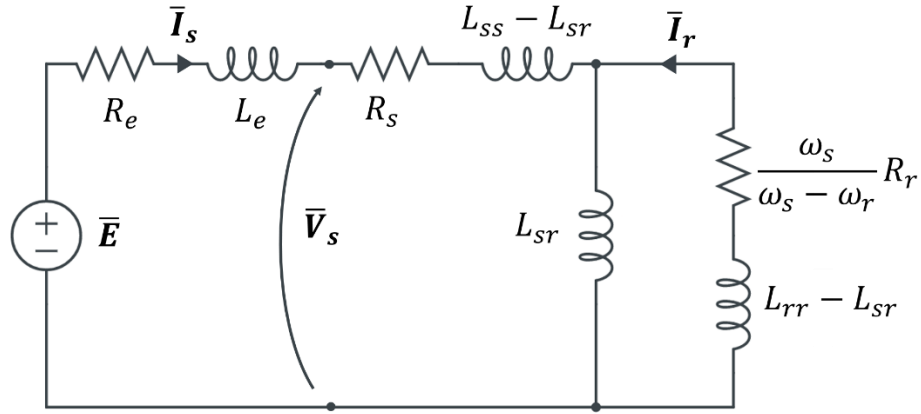


Figure 11: Induction motor model as an AC circuit

The phasors equations (42) to (46) lead to the AC circuit drawn in Figure 11. Once all resistances and inductances of this circuit are identified (i.e knowing  $\omega_s$ ,  $\omega_r$  and the pump parameters), the 10 previously cited unknowns can be computed.

### 2.2.2 Numerical resolution

The governing equations introduced in the previous subsection is solved via the procedure described in Figure 12. The solver needs the inputs (Table 7) as well as the parametrisation of the pump (Table 5) to compute the unknowns (Table 8). Three important steps should be performed before applying a general Newton Raphson algorithm (required because of non-linear equations). First, special cases should be analysed in S-1. The program checks also that the motor is not stall in S-2. Otherwise, the pump is certainly oversized compared to the motor in terms of mechanical torque required. Ultimately, since a guess of the unknowns are used to start the resolution, the next step is to identify a suitable guess for the unknowns in S-3. A suitable guess is not obvious. During this step, the feasibility of the pump parameters is discussed and error messages are triggered when coefficients lead to unfeasible cases. Afterwards, the governing equations could be solved through a Newton-Raphson algorithm in S-4. Each steps are detailed below.

In S-1, two cases are analysed: a zero input voltage or a zero input frequency. If the voltage applied to the pump is zero, no current is provided in the stator, no magnetic field is induced and thereby, no rotation is initiate. It results thereby to all unknowns equal to zero. If only the frequency applied is zero, the current present in the stator windings are direct (DC current). It implies that the stator magnetic field created is fixed and does not rotate. The rotor windings are not submitted to a varying magnetic field, no current is induced and thus, no torque is applied to the rotor (meaning no rotation of the pump:  $\omega_r = 0$ ). The pump head and its flow rate are equal to 0. Concerning the electrical unknowns, those can be found by solving the phasor circuit introduced in the previous subsection.

In S-2, a verification is performed to assess if the motor may be stall. If the load torque ( $T_{fr} + T_p$ ) for a zero flow rate corresponding to a start-up is lower than the maximum electric torque  $T_{e,max}$  for the rotation speed  $\omega_{r,max}$ , then the motor is considered stall and is not operating in its range. This may occur for example if the pump design does not suit with the power capacity of the motor.

In S-3, the initialisation of the unknowns is computed to start afterwards a Newton Raphson algorithm to solve the governing equations. To designate these initialised values, a  $I$  subscript is used. Hence, the flow rate is first initialised to 0:  $Q_I = 0$ .

The substep S-3-1 consists to compute the rotation speed  $\omega_{r,I}$  based on an new assumption. The electric torque is linearized around the synchronous speed  $\omega_s$ . The linearization is given in (47) and is

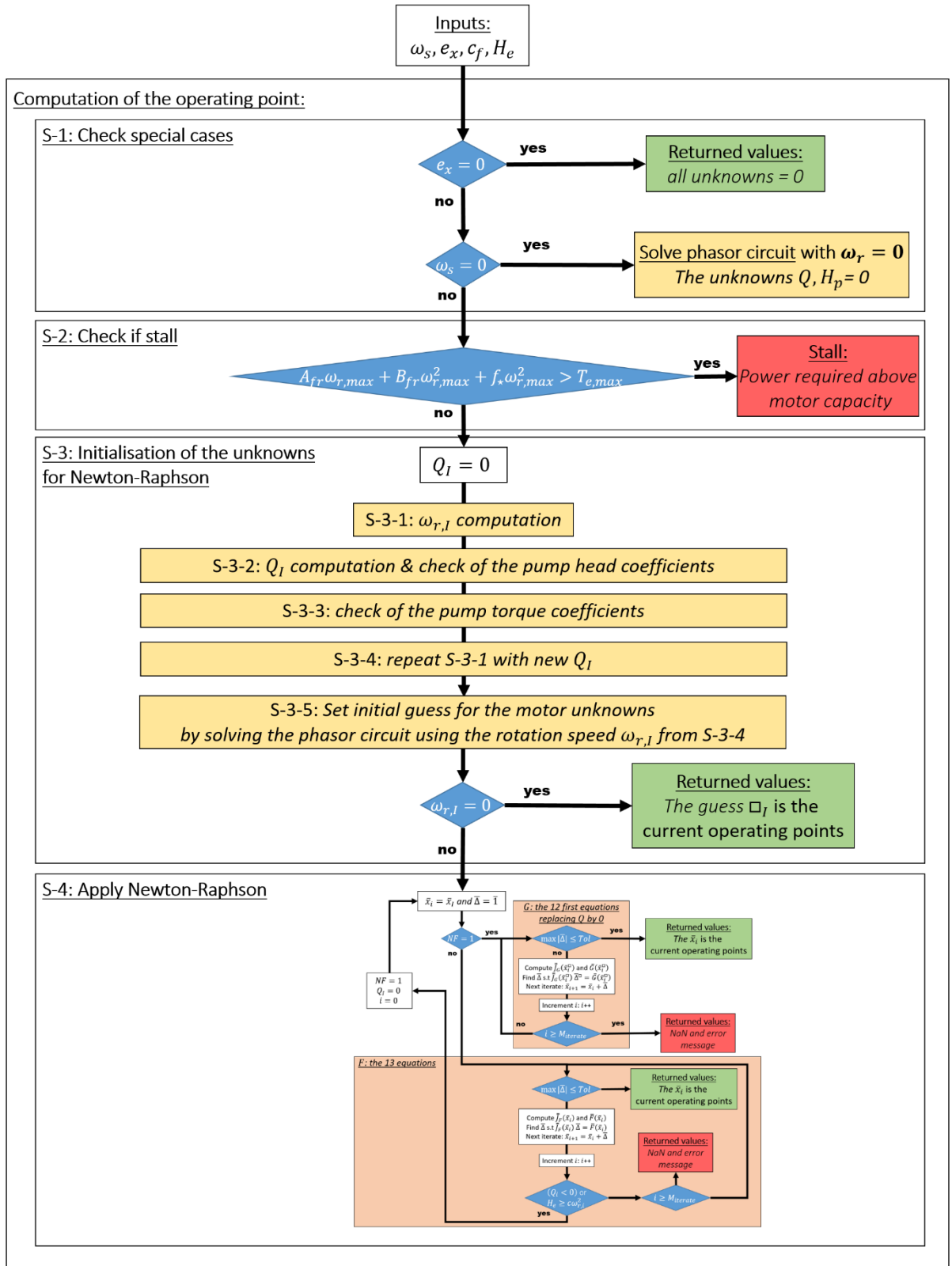


Figure 12: Numerical resolution diagram: blue rhombus contain logical expression to guide the numerical resolution; green boxes refer to the returned unknowns; red boxes stand for error cases; yellow boxes are processes that are detailed in the report; white boxes are calculations

illustrated in Figure 13. Then, the rotation speed can be estimated by solving (48) analytically that is obtained by substituting (47) in (33). The solver takes into account the possibility that both coefficients  $B_{fr}$  and  $f_*$  are equal to zero. If two solutions exist, the solver takes the greatest rotation speed.

$$T_e(\omega_{r,I}) \approx \frac{NT_e}{c_{Te}} (\omega_s - \omega_{r,I}) \quad (47)$$

$$(B_{fr} + f_*)\omega_{r,I}^2 + \left(\frac{NT_e}{c_{Te}} + A_{fr} + eQ_I\right)\omega_{r,I} + dQ_I^2 - \frac{NT_e}{c_{Te}}\omega_s = 0 \quad (48)$$

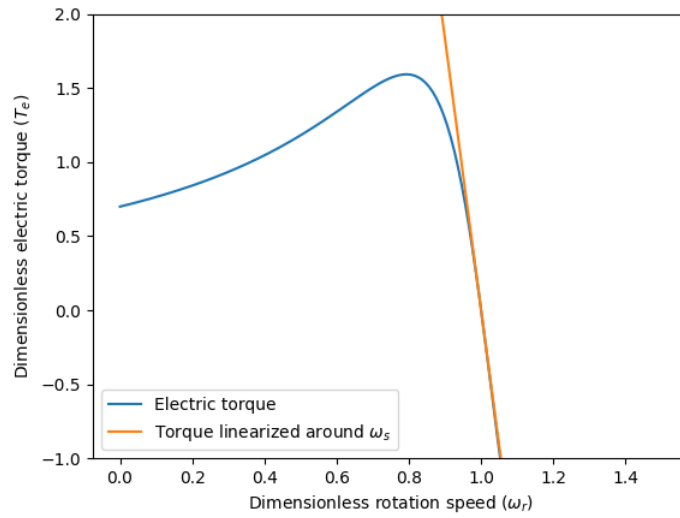


Figure 13: Electric torque curve and its linearization to find an approximation of the operating rotation speed

In the next substep S-3-2, the pump flow rate is estimated based on the rotation speed  $\omega_{r,I}$  and the coefficients characterising the pump head are discussed. This step is described in Figure 14. If  $a = 0$ , since the pump head decreases with the flow rate, it means  $b < 0$  must be satisfied. Two cases are then analysed:  $a < 0$  or  $a > 0$ . The pump head has a negative (resp., positive) concavity and its maximum head should correspond to a negative (resp., positive) flow rate  $Q_{max} = -\frac{b}{2a}\omega_r \leq 0$  (resp.,  $Q_{max} > 0$ ). So, it implies  $b \leq 0$ . If  $a < 0$  (resp.,  $a > 0$ ), the operating part of the curve is located on

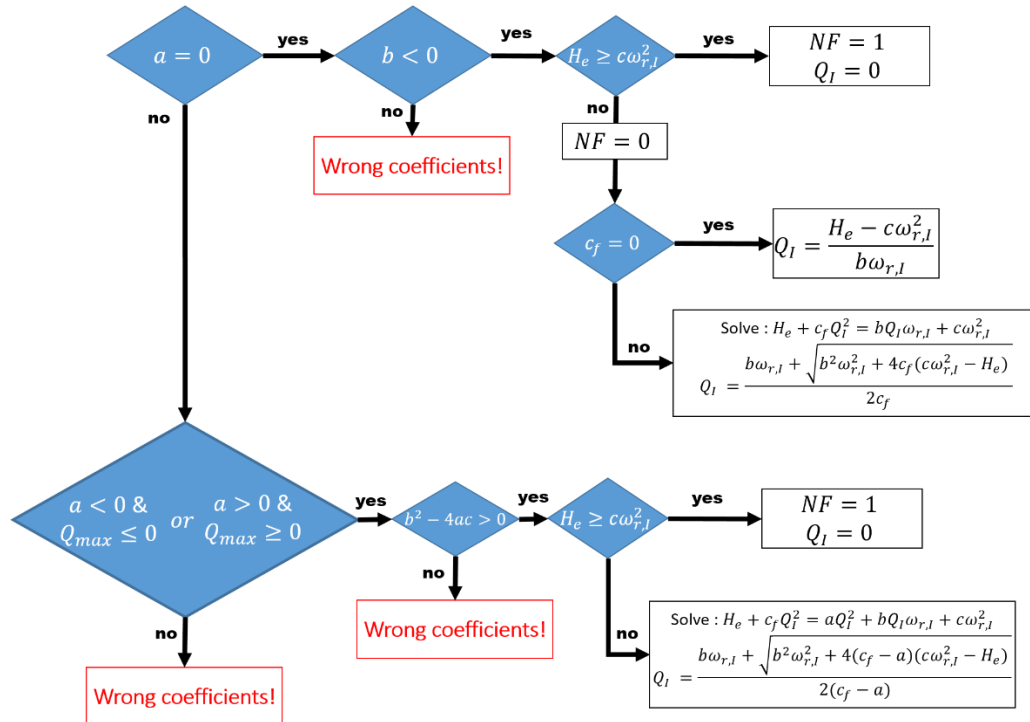


Figure 14: Logic diagram of the flow rate computation for initialisation (step S-3-2)

the right (resp., left) side of the maximum (resp., minimum). Furthermore, the pump head should cross the flow rate axis:  $b^2 - 4ac > 0$ . This is ensured for  $a < 0$  by the fact that the head corresponding to  $Q = 0$  should be positive implying  $c > 0$ . A binary number  $NF$  is introduced and is equal to 1 if there is no flow rate. The flow condition is  $H_e < c\omega_r^2$ . If not satisfied, it means either that the pump is downsized compared to its use or that the pump is rotating at a too small rotation speed. Ultimately, the flow rate  $Q_I$  is obtained by solving the general equation (49) in all cases described above.

$$H_e + c_f Q_I^2 = a Q_I^2 + b Q_I \omega_{r,I} + c \omega_{r,I}^2 \quad (49)$$

The substep S-3-3 consists to check the consistency of the pump torque coefficients and is described in Figure 15. The concavity of both load torques should be positive or zero. The zero of the combined load torque (50) as a function of the rotation speed should occur for a rotation speed lower than the synchronous speed  $\omega_s$ . It is ensured in a case of a parabolic combined load torque if  $e > 0$ . In a case with linear expression of the combined load torque with respect to the rotation speed, if  $d \geq 0$ , it is ensured while otherwise, the zero should be evaluated and compared to  $\omega_s$ .

$$T_{fr} + T_p = d Q_I^2 + (A_{fr} + e Q_I) \omega_{r,I} + (B_{fr} + f_*) \omega_{r,I}^2 \quad (50)$$

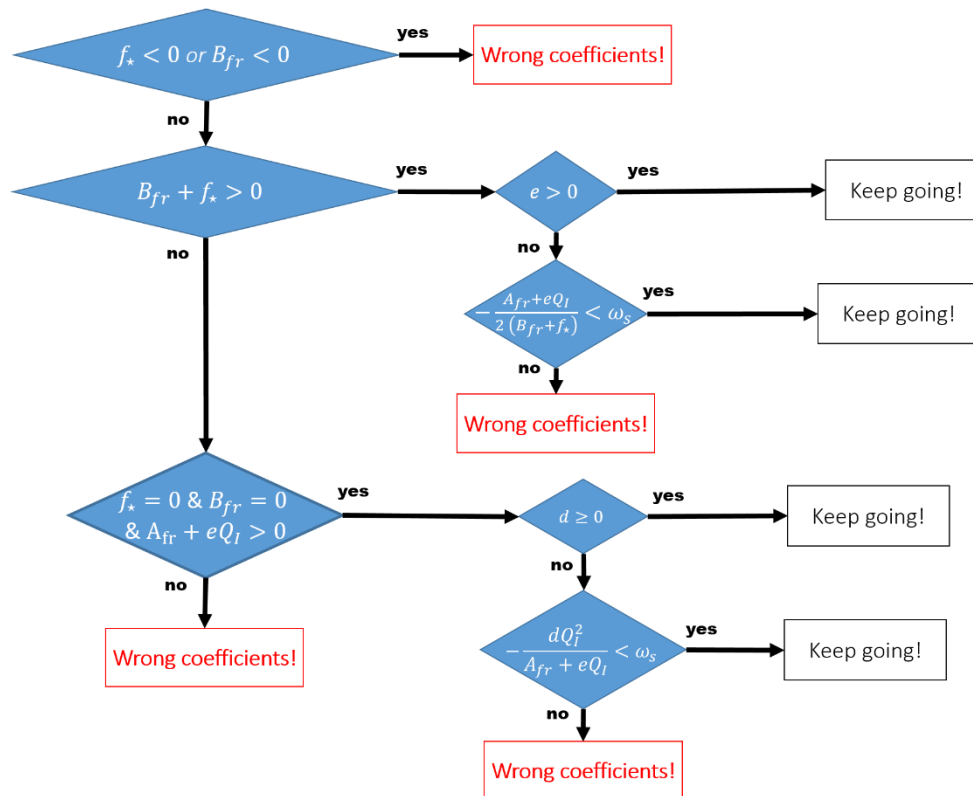


Figure 15: Logic diagram to assess the consistency of the pump torque coefficients

A new rotation speed is computed at the substep S-3-4 by solving (48) with the previous flow rate  $Q_I$  (from S-3-2). At this stage, good initial values are obtained for the flow rate and the rotation speed. As matter of the head, one initial value is obtained easily by computing (12) with  $Q_I$  and  $\omega_{r,I}$ . The ten lasts unknowns to initialise can be estimated by solving the AC circuit with the rotation speed  $\omega_{r,I}$  (Substep S-3-5). Then, if the initialised rotation speed obtained is zero, it means no flow rate and no pump head. The non-linearity of the system disappears and the initialised unknowns correspond to the real state of the pump. If the initialised rotation speed obtained is different from zero, the motor

is rotating leading to a potential flow rate and the electric torque non linearity implies a Newton-Raphson algorithm to solve the governing equations.

The initialised values of the unknowns are gathered to  $\bar{x}_1$  and passed as the first iterate  $\bar{x}_i$  of a Newton-Raphson resolution (S4). The process is detailed in Figure 16. The iterate increment vector  $\bar{\Delta}$  is initialised to a unity vector and represents the difference  $\bar{x}_{i+1} - \bar{x}_i$ . Then, depending if a flow rate occurs ( $NF = 0$ ) or not ( $NF = 1$ ), the system of equation is different. If  $NF = 1$ , the (13) does not make sense anymore. The 12 governing equations replacing  $Q$  by 0 are then gathered under the system  $\bar{G}$ . The general Newton-Raphson algorithm is applied to the system  $\bar{G}$  with  $\bar{J}_G$  denoting the Jacobian matrix of  $\bar{G}$ . A new operator is defined the power  $\square$ . This operator takes its base, a vector element and return this vector without its last element. The last element of  $\bar{x}_i$  is the flow rate. Thereby,  $\bar{x}_i^\square$  stands for the 12 unknowns and the 13<sup>th</sup> element of  $\bar{x}_i$  is zero. If  $NF = 0$ , the 13 governing equations are used and gathered under the system  $\bar{F}$ . Inside the loop that performs the Newton-Raphson algorithm, the flow rate and the flow condition are assessed at each iterate  $i$ . If the flow rate is negative or zero, then, it means that the current operating point is certainly with a zero flow rate conversely to the first guess obtained by the computation of  $Q_i$ .  $NF = 1$ , and the Newton-Raphson algorithm is restarted with the smaller system  $G$  and a zero flow rate.

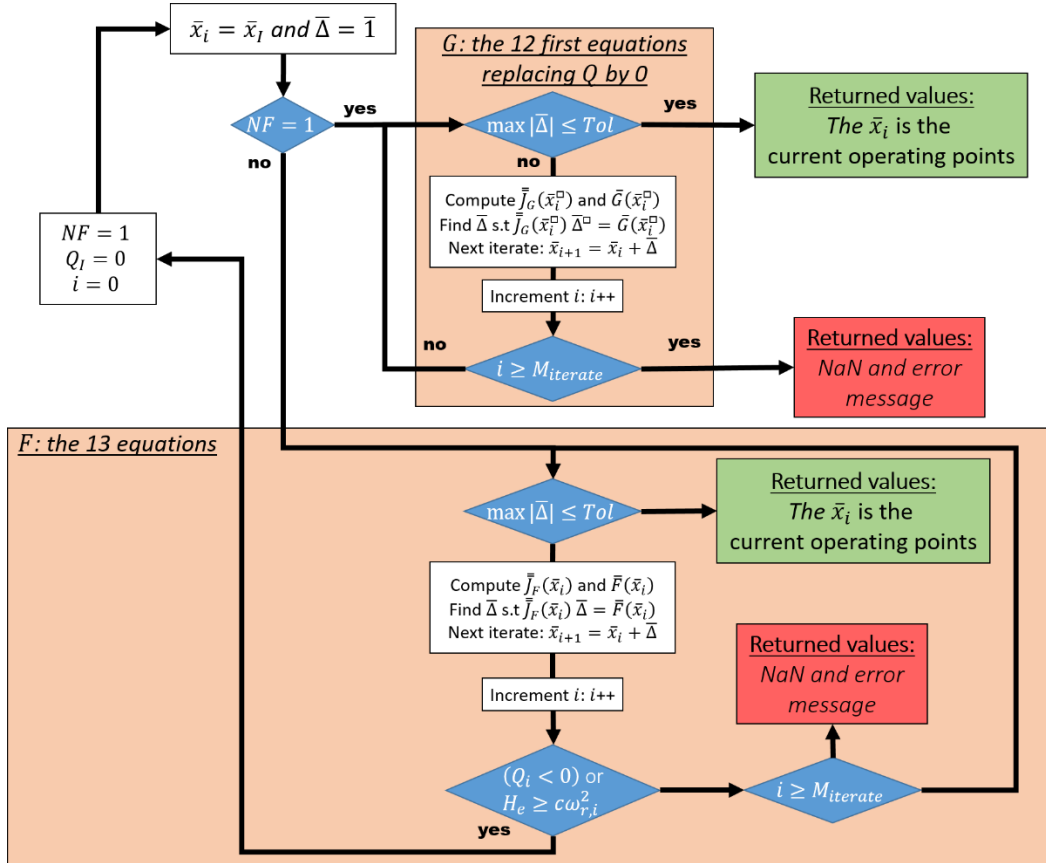


Figure 16: Newton-Raphson algorithm applied to solve the governing equations in the general case

After all, the accuracy of the solution is tuned by a tolerance value  $Tol$  and the solver is also equipped with a stopping criterion if the number of iterations reaches  $M_{iterate}$ . The default values for these two numerical parameters are provided in Table 9. The solver is used in an example in Figure 17 and two criteria are displayed to check its convergence and the errors: the maximum of the absolute values of the increment vector; and the maximum of the absolute values of the system  $F$  which should tend to 0. As seen, after a few iterations the solution obtained is pretty good and a tolerance of  $1e-9$  is reached in four iterations leading to an approximate error of  $1e-14$ . To solve this kind of non-linear

system in a so few steps is quite remarkable and is a huge help for further implementations since the model should be calibrated based on experimental data for 12 coefficients.

$Tol$	1e-9	$M_{iterate}$	2000
-------	------	---------------	------

Table 9: Default parameters of the solver to obtain pump operating points

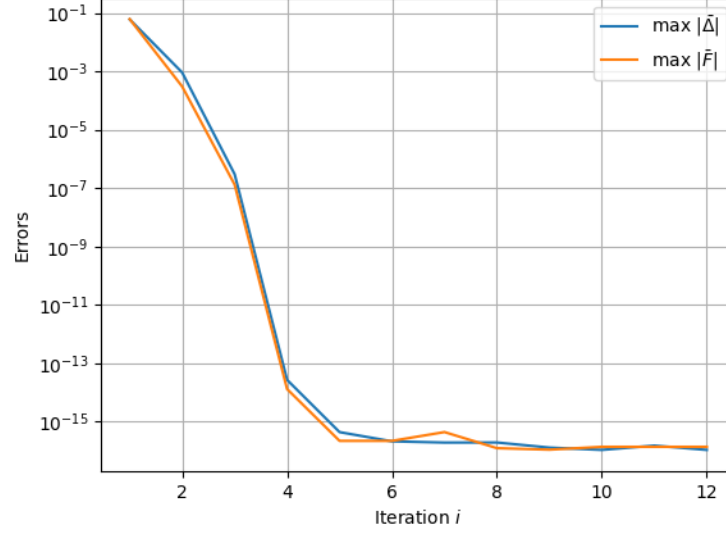


Figure 17: Convergence of the solver in terms of increment vector and the remains of the system  $F$  for the following inputs ( $\omega_s = e_x = 1$ ;  $c_f = 0$  and  $H_e = 0.75$ ) and parameters

$$([R_s, R_r, L_{ss}, L_{sr}, L_{rr}, A_{fr}, B_{fr}, a, b, c, d, e, f_*] = [0.1; 0.06; 2.14; 2.06; 2.15; 0.1; 0.0; -0.15; -0.29; 0.96; -0.17; 0.3; 0.39])$$

### 2.2.3 Calibration procedure

The calibration of the numerical model is performed based on a non-linear home-made optimisation technic, namely the interior point method using the gradient as the direction and a Nelder-Mead optimisation method to find the appropriate step. The goal of the calibration is to find the parameters of the model leading to numerical outcomes as close as possible to the real operating conditions measured during a pump test. Based on the conducted measurements, it is impossible to identify separately the coefficients  $B_{fr}$  and  $f_*$ . As shown in (11), only their sum can be identified. For the sake of simplicity, we set here  $B_{fr}$  to 0 and we consider only parameter  $f_*$ .

The method requires an initial guess of parameters given in Table 10. The subscript  $\square_{app}$  denotes an approximation of the coefficients  $a \rightarrow f_*$ . The six first parameters are arbitrarily chosen within their standard range of variation as given in Table 6. A relatively low value was taken for coefficient  $A_{fr}$  which represents motor internal friction. Since all quantities are dimensionless in the numerical model, the measurements recorded in a pump test are divided by their corresponding basis ( $Q_B$  and  $S_B$ ) and denoted by the upper script  $\square^*$ .

$R_s$	$R_r$	$L_{ss}$	$L_{sr}$	$L_{rr}$	$A_{fr}$
0.02	0.02	2.2	2.1	2.2	1e-4
$a$	$b$	$c$	$d$	$e$	$f_*$
$a_{app}$	$b_{app}$	$c_{app}$	$d_{app}$	$e_{app}$	$f_{app}$

Table 10: Initial guess of the numerical model parameters for the calibration procedure

The initial guess  $a_{app}, b_{app}, c_{app}, d_{app}, e_{app}$  and  $f_{app}$  are obtained based on these two assumptions:

$$\omega_r = 0.9 \omega_s^* \quad (51)$$

$$T_p = \frac{P_e^*}{\omega_s^*} \quad (52)$$

These equations are valid for operation conditions close to the nominal ones. Thereby, the rotation speed is almost equal to the synchronous speed and the motor efficiency is considered as 90%, which leads to (52). The efficiency of variable speed drive is assumed equal to 100 % because of its relatively high efficiency [16]. Introducing these assumptions into (18) and (12) enables ending up with a set of linear expressions, which can be solved for the coefficients using a linear least square method:

$$H_p^* = a_{app}(Q^*)^2 + b_{app}Q^*0.9\omega_s^* + c_{app}(0.9\omega_s^*)^2 \quad (53)$$

$$\frac{P_e^*}{\omega_s^*} = d_{app}(Q^*)^2 + e_{app}Q^*0.9\omega_s^* + f_{app}(0.9\omega_s^*)^2 \quad (54)$$

Next, a non-linear optimization problem is solved to calibrate the numerical model based on  $N_p$  measured operating points. The objective function is:

$$\min \theta(\bar{x}_p) = \sum_{l=1}^{N_p} c_Q(Q_l - Q_l^*)^2 + (1 - c_Q)(e_{x,l}i_{qs,l} - P_{e,l}^*)^2; \quad (55)$$

where the subscript  $l$  refers to the measurements and the equivalent outcomes of the numerical model for a same input configuration  $(\omega_{s,l}^*, H_{p,l}^*)$ , from 1 to  $N_p$ . The inputs for each measurement are given as  $(\omega_s = \omega_{s,l}^*; e_x = \omega_{s,l}^*; H_e = H_l^*; c_f = 0)$ . The objective function (55) aims at minimising a weighted sum of the squared flow rate deviation of the numerical model from the experimental measurements and the squared power consumption deviation. Coefficient  $c_Q$  varies in the interval  $[0, 1]$  and is a parameter of the optimisation. It plays the role of a weight to prioritize the accuracy of the flow rate compared to the power consumption or vice-versa. The numerical model called  $N_p$  times could have been considered as equality constraints. Nevertheless, as this amount of equality constraints (11 equations for all  $N_p$  measurements leading to  $11N_p$  equations) are huge, they are not considered in the optimization process to build the Lagrangian function. Instead, the only variables of the optimisation are the model parameters  $\bar{x}_p = (R_s, R_r, L_{ss}, L_{sr}, L_{rr}, A_{fr}, a, b, c, d, e, f_*)$ . For each optimisation iteration, the numerical model is called with model parameters corresponding to the iterate of the optimisation process for all  $N_p$  configurations.

The inequality constrains are:

$$\bar{c}(\bar{x}_p) \geq \bar{0} \quad \left\{ \begin{array}{ll} 0.01 < R_s < 0.12 & (56) \\ 0.01 < R_r < 0.12 & (57) \\ 0.07 < L_{ss} - L_{sr} < 0.15 & (58) \\ 1.8 < L_{sr} < 3.8 & (59) \\ 0.06 < L_{rr} - L_{sr} < 0.15 & (60) \\ 0 < A_{fr} < 0.2 & (61) \\ 0 < a/a_{app} < 2 & (62) \\ 0 < b/b_{app} < 2 & (63) \\ 0 < c/c_{app} < 2 & (64) \\ 0 < d/d_{app} < 2 & (65) \\ 0 < e/e_{app} < 2 & (66) \\ 0 < f_*/f_{app} < 2 & (67) \end{array} \right.$$

and can be gathered under the notation  $\bar{c}$ . The fives first inequalities comes from the literature [17]. Equation (61) is a relatively large interval that hardly influences the optimisation as the actual value of  $A_{fr}$  is expected to remain low (since it expresses the rotational friction inside the motor). The bounds of the last six coefficients are fixed arbitrarily to twice the approximated coefficients obtained by applying the least square identification method according to (53) and (54). This last choice offers a quite large range of variation for these six coefficients and should be enough since the approximations obtained  $\square_{app}$  are probably not far from the real coefficients that the calibration should return.

In terms of resolution, four additional coefficients are introduced to guide the calibration. Hence, five coefficients may influence the way the optimisation under constraints behaves. These are described in Table 11. The optimisation technic performed is described in Figure 18. Ultimately, at the end, an optimisation is performed **without constraints** with as guess, the final  $\bar{x}_p$  obtained in the calibration under constraints.

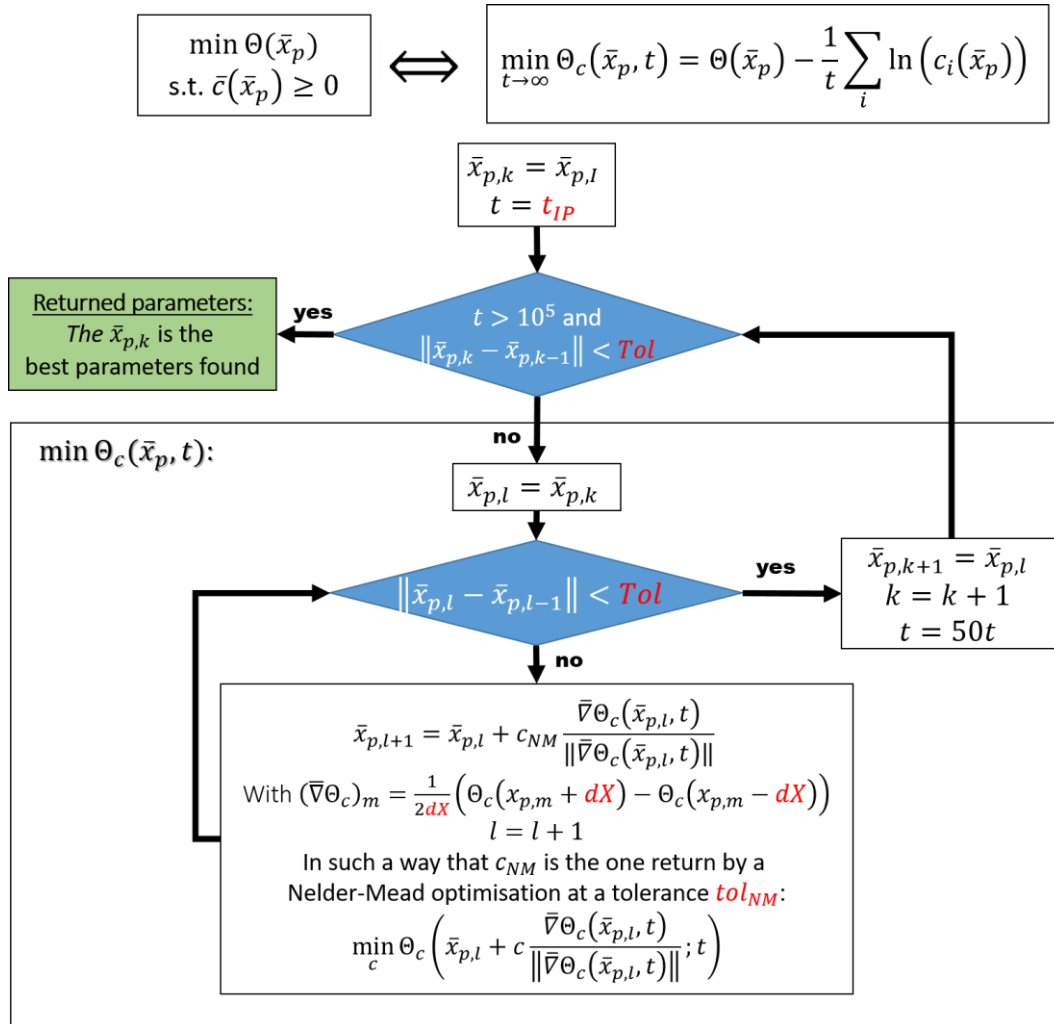


Figure 18: Numerical resolution of the calibration problem emphasizing the role of each computational parameters of Table 11

Notation	Default value	Signification
$c_Q$	0.5	Homotopy coefficient that varies in the interval [0, 1] and is a parameter of the objective function. It plays the role of a weight to prioritize the accuracy of the flow rate compared to the power consumption when greater than 0.5
$Tol$	1e-4	It gives the tolerance at which the optimization could stop. The criterion is: $\ \bar{x}_{p,i} - \bar{x}_{p,i-1}\  < Tol$
$t_{IP}$	100	This parameter is the first gain applied to the constrains. The smaller the more the constrains influence the direction of the path to the best parameters $\bar{x}_p$ .
$dX$	1e-7	The variation of parameter used to estimate the derivative of the objective function with respect to the parameters. Fortunately, since the numerical model is dimensionless, a same variation could be used for each parameters.
$Tol_{NM}$	1e-7	The tolerance that the Nelder-Mead method should have to estimate the optimal step to approach a minimum.

Table 11: Parameters of optimisation to calibrate the pump model

## 2.2.4 Uncertainties estimation

This section details the uncertainties on the experimental measurement and on the computational model calibrated. The experimental uncertainties are coming from the head measurement. Indeed, to make it simpler and inexpensive, the head measurement is performed outside of the tank (for submersible pumps) which results to decrease the pump head measurement, by the head losses. Uncertainties variables are then introduced for the computational model. They allow assessing the performance of the computational model to mimic pump operation.

The uncertainties on the experimental measurement is firstly discussed. The real head measurement  $H_p^*$  is given by:

$$H_p^* = H_p + H_{p,loss} \quad (68)$$

where  $H_{p,loss}$  stands for the head losses between the pump discharge and the four point pressure measurement displayed by blue lines in Figure 19. During the calibration,  $H_{p,loss}$  is assumed negligible. The error on the head could be estimated by:

$$\tau_H = \frac{H_{p,loss}}{H_p^*} \quad (69)$$

The losses  $H_{p,loss}$  can be estimated thanks to [5] and [15]. The head losses include these components: three elbows DN350 (3mm thick), 939.7 mm of straight pipe, a 248mm long reduced section from DN250 to DN350 and a 200mm long rubber compensator. The error on the head is displayed in Figure 20.b). The main observations are that the error on a 5m head is about 0.5m for very high flow rate (300 l/s), around 0.2m for 200 l/s, and for lower flow rate, really negligible. As a result, one can assume the measurement  $H_p^*$  to be equal to the actual pump head  $H_p$ . Figure 20.a) illustrates that the most part of head losses come from the three elbows.

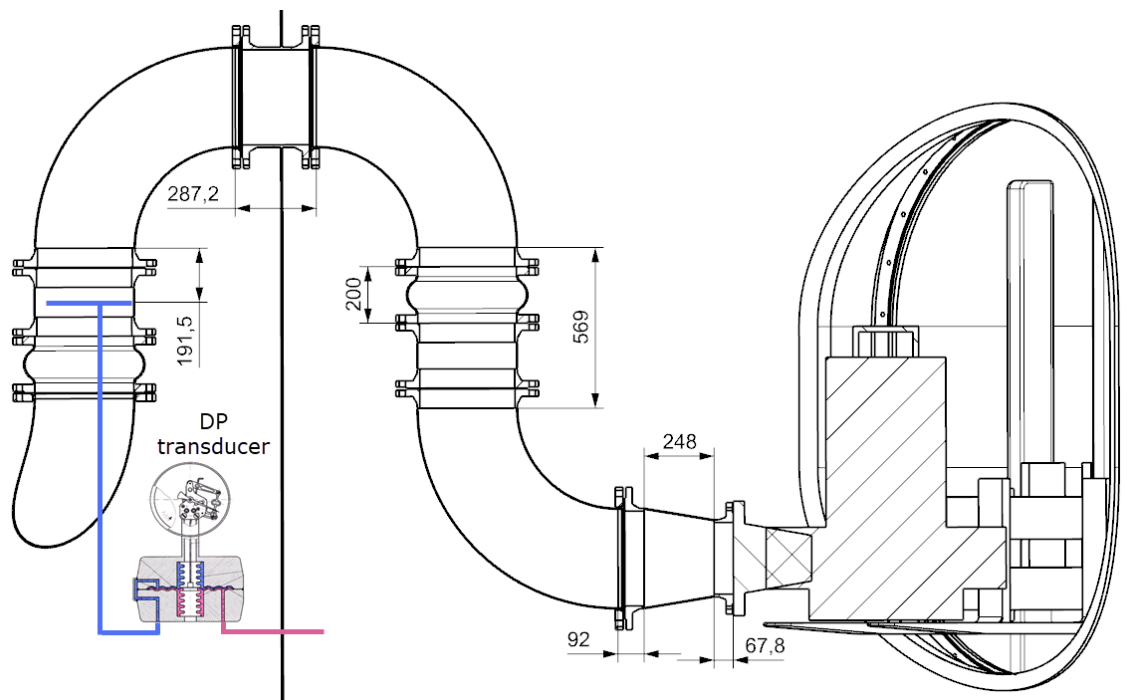


Figure 19: Submersible pump discharge and pressure measurement

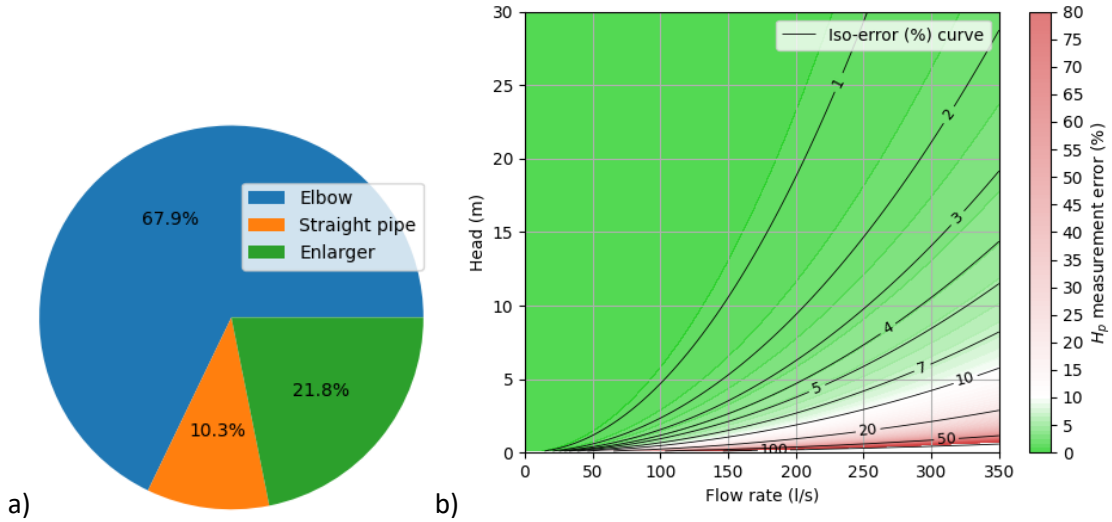


Figure 20: a) Components contribution to the total head losses ; b) Errors on the head measurements corresponding to different flow rates

The uncertainties link to the numerical model calibrated is evaluated by the RMS and the standard deviation of the relative errors on the flow rate, the electric power and the efficiency given by:

$$\bar{r}_{P_e} = \frac{\bar{P}_e - \bar{P}_e^*}{\bar{P}_e^*} ; \quad (70)$$

$$\bar{r}_Q = \frac{\bar{Q} - \bar{Q}^*}{\bar{Q}^*} ; \quad (71)$$

$$\bar{r}_\eta = \frac{\bar{\eta} - \bar{\eta}^*}{\bar{\eta}^*} . \quad (72)$$

The bar  $\bar{\quad}$  stands to gather all values corresponding to one test in a vector. The RMS and the standard deviation are computed for these three samples in the result section and offer a good approach to estimate the accuracy of the computational model.

## 2.2.5 Software implementation

To update Later

The numerical model introduced in the previous subsection, is used in a graphical user interface coded in python to provide operating information to the user for a given configuration frequency and voltage applied to the motor, as well as the head difference required and the flow coefficient of the suction/discharge pipe. Figure 21 shows the toolkit with two tabs and a “File” menu. The first tab gives the characteristics of the pump and should be entered by the user. It is composed of five boxes. The “Motor” box contains the coefficients related to the motor: (1) to (9); and (17). The “Pump” box contains the coefficients related to the pump: (12) and (18). The “Nominal characteristics” box contains the nominal characteristics used to build the basis to render the numerical problem dimensionless. The example displayed in Figure 21 a) correspond directly to the data of the pump n°1 for the “Nominal characteristics” box and to the coefficients resulting from the calibration process for the “Motor” and “Pump” box. The calibration process is based on experiments in the test bench and is detailed in the section 2.2.3. The inputs to the numerical model are contained in the “Hydraulic configuration” box and the “Motor control” box and should be passed with dimension. The “Hydraulic configuration” box contains the required head difference in meter (i.e, the head difference between the free-surface of navigation reach at the inlet and the free-surface of navigation reach at the outlet) and the flow coefficient (with dimensions) modelling the sum of head losses present in the suction

and discharge piping. The flow coefficient is defined such a way that the head losses (in [m]) equal to the flow coefficient times the square of flow rate (in [m<sup>3</sup>/s]). To obtain the coefficient  $c_f$  dimensionless, the toolkit multiplies the user flow coefficient by  $Q_B^2/H_B$ . The “Motor control” box contains the user voltage ( $e_x = 400/V_B$ ) and frequency ( $\omega_s = 50/f_B$ ). Using a speed drive or a variable frequency drive, these values can be chosen by the user. Yet, depending on the control technique, a relation is imposed between the voltage and the frequency. A famous one is the scalar control that imposes a constant maximum torque for the motor torque curve (electric torque vs rotation speed). Many popular thoughts leads to the ratio  $V/f$  constant to achieve the scalar control. Unfortunately, since the stator windings present generally a resistance and an inductance not negligible, this ratio does not lead to the goal of the scalar control ([19]). The ratio  $V^2/f$  leads to better result and should be privileged. The button ‘Scalar:  $V^2/f = cst$ ’ serves this purpose. A push on this button compute automatically the input voltage and replace it to ensure the ratio  $V^2/f$  is constant.

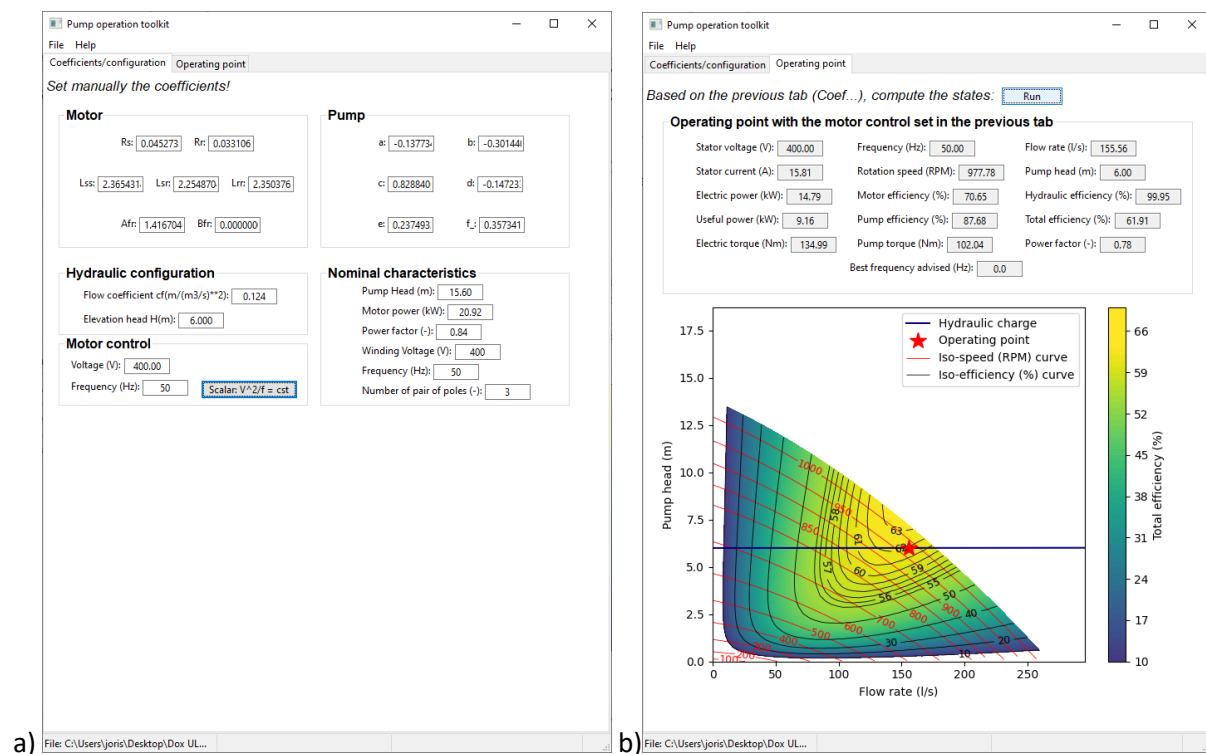


Figure 21: Pump operation toolkit: model coefficients and inputs (a); Operating point (b)

The File menu may be used to import the characteristics of one pump (by the use of the shortcut Ctrl-O or the “File” menu, Figure 22), save their characteristics in a CSV file and save several operating points in a CSV file.

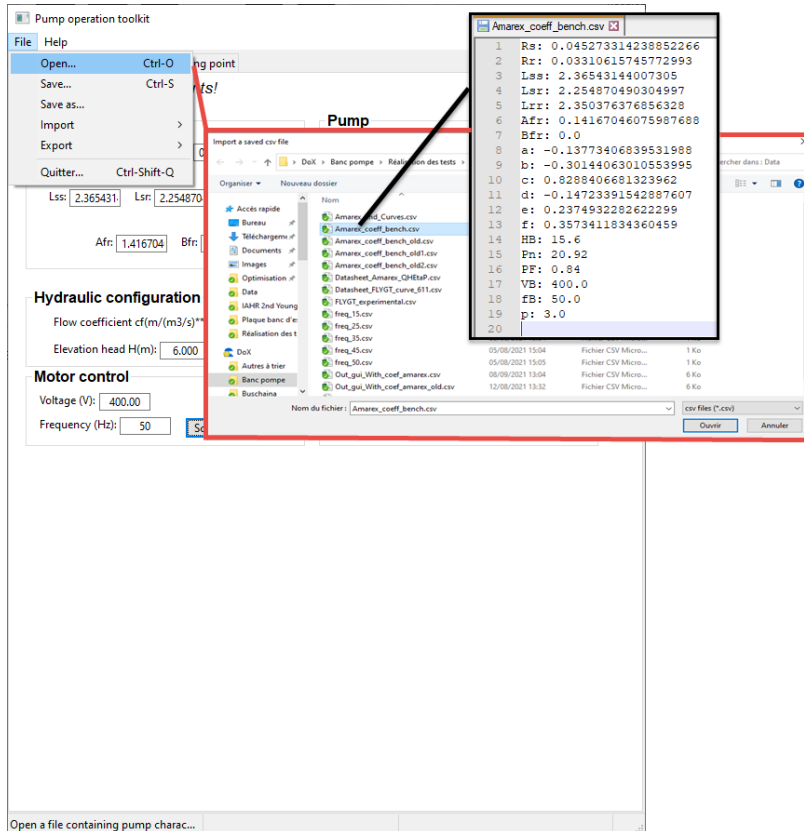


Figure 22: Opening of a file in the pump operation toolkit

Figure 23: Save of several operating points in a file with the pump operation toolkit

## 2.2.6 Study examples

**Example 1:** pumping station with a 6-meter head difference, a head losses coefficient of  $50 \text{ m}/(\text{m}^3/\text{s})^2$  and a motor full fed (50 Hz, 400 V)

Based on the configuration of the example and the excitation of the motor, the dimensionless inputs can be deduced:

$$\omega_s = \frac{50}{f_B} = 1 \quad (73)$$

$$e_x = \frac{400}{V_B} = 1 \quad (74)$$

$$H_e = \frac{2.3}{H_B} = 0.14 \quad (75)$$

$$c_f = 50 \frac{Q_B^2}{H_B} = 0.085 \quad (76)$$

Figure 24 a) shows the corresponding configuration to enter as inputs of the numerical model in the pump operation toolkit. Then, the computation is performed by clicking on “Run” button in the second tab (“Operating points”). The results are displayed in the box “Operating point with the motor...” and in a graph relating the pump head as function as the flow rate. This graph shows the operating point in star, the hydraulic charge curve corresponding to the head difference and the head losses proportional to the square of the flow rate. The iso-efficiency curves are also displayed corresponding to a VFD strategy of constant  $V^2/f$ . These curves are obtained by varying the rotation speed and the pump head. The tool returns also the best frequency advised to retrieve the highest

efficiency for a specific hydraulic configuration (given by the user in the first tab). In this example, the best frequency advised is 46.85 Hz. With this excitation, one expects an improvement of the total efficiency from 54.34 % to 55.11% (Figure 25).

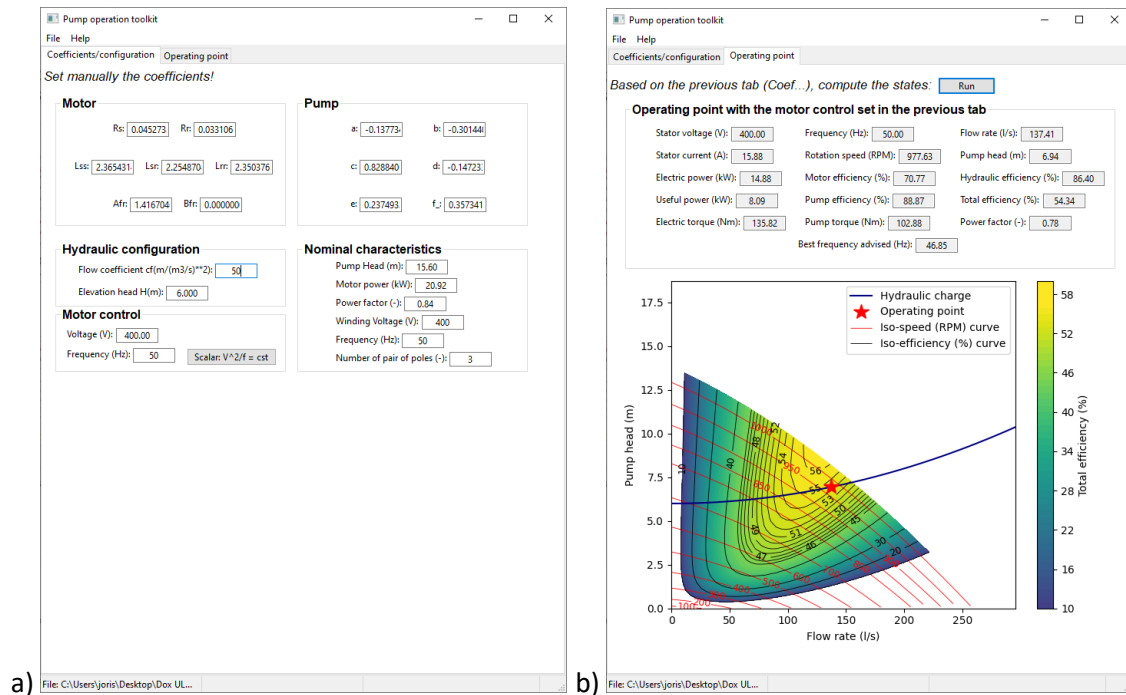


Figure 24: Example 1 applied on the pump operation toolkit

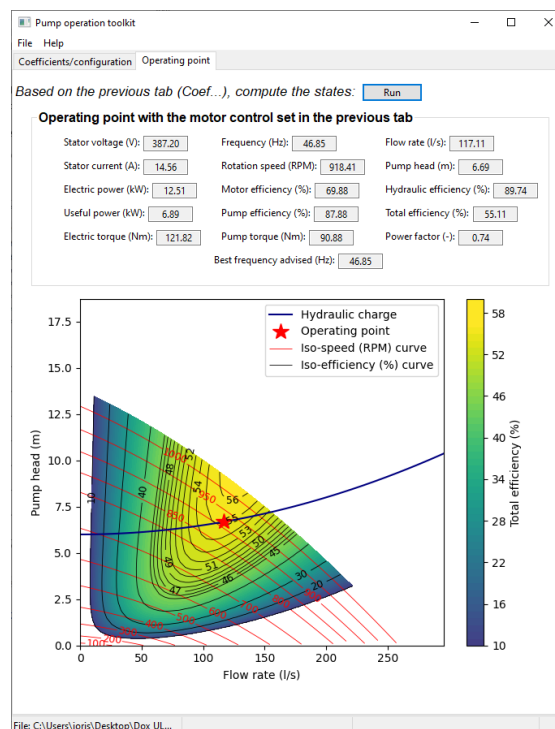


Figure 25: Example 1 applied on the toolkit with the best frequency advised

Example 2: in context of the test bench, one measurement: 50 Hz, 2.3 m, 222 l/s, 14 kW

The efficiency of the assembly motor/pump can be evaluated:  $(\rho g H_p Q) / P_e = 1000 * 9.81 * 2.3 * 0.222 / 14000 = 35.8 \%$ . To compute this operation point with the pump operation toolkit, the

following inputs should be applied: 50 Hz, 400 V, and a head difference of 2.3 m (without any flow coefficient:  $c_f = 0$ ).

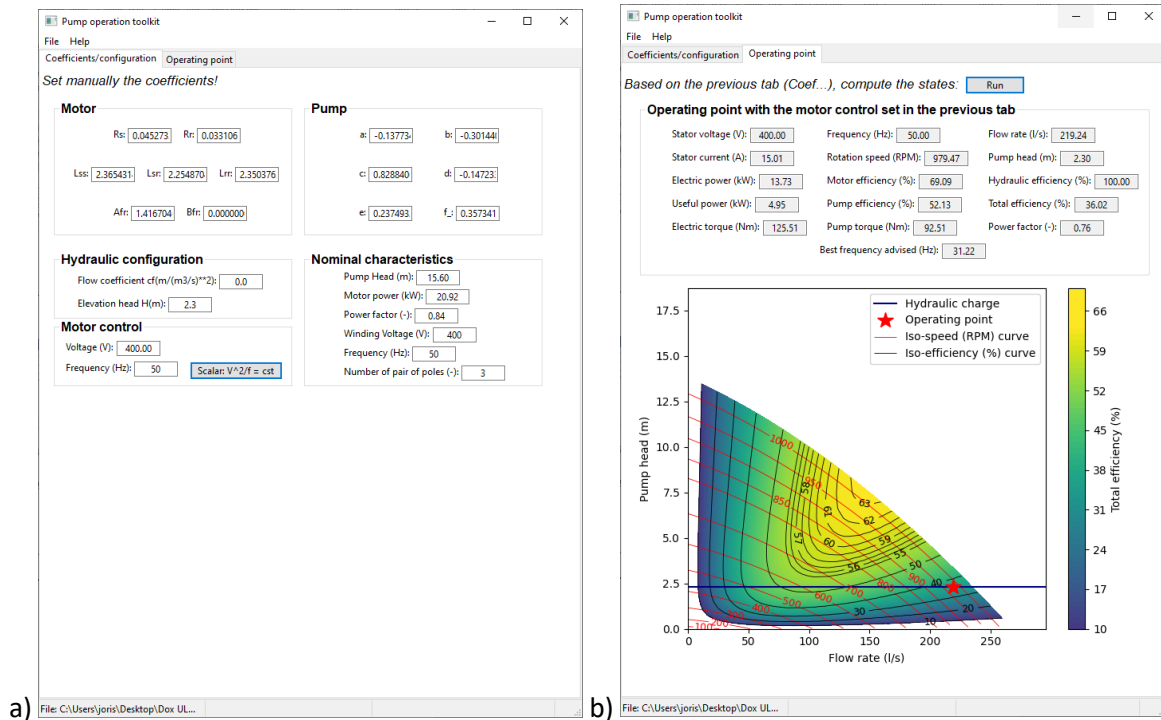


Figure 26: Example 2 applied on the pump operation toolkit

The variable computed by the model can then be compared to the measurement to evaluate the confidence to the model. The head and the frequency are directly applied. The flow rate and the electric power retrieved are respectively 219.24 l/s and 13.73 kW. Comparing also the efficiency, the numerical model leads to 36%. It proves the good confidence of the numerical model.

## 2.3 Tested pumps

### 2.3.1 Pump 1: Amarex KRTK 250 - 400/206UG-S

The main operating characteristics of the pump is listed in Table 12 and documented in [8]. The technical drawing of the pump is displayed in Figure 27. It is to note that no lifting bail was delivered with the pump. The pump curves provided by the datasheet is shown in Figure 28.

Flow rate	170 l/s	Nominal voltage	400 V
Head	6.00 m	Nominal frequency	50 Hz
Operating speed	965 RPM	Nominal electrical power	18 kW
Absorbed power	14.03 kW	Nominal current	35.5 A
Efficiency	71.7 %	Nominal efficiency	87 %
Number of pair of poles	3	Nominal power factor	0.85

Table 12 : Operating characteristics of the 'Amarex KRT D 250 - 400/206UG-S' pump.

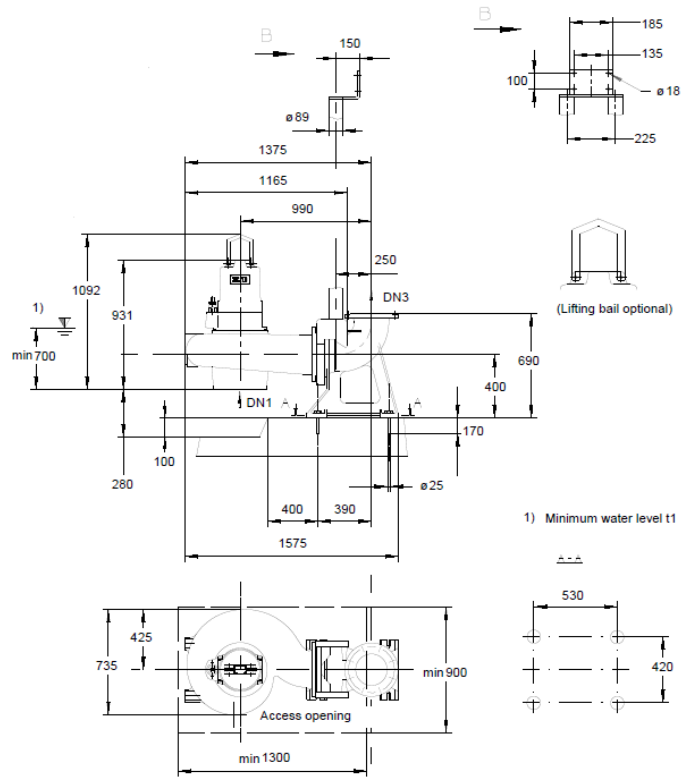


Figure 27: Technical drawing of the Amarex pump

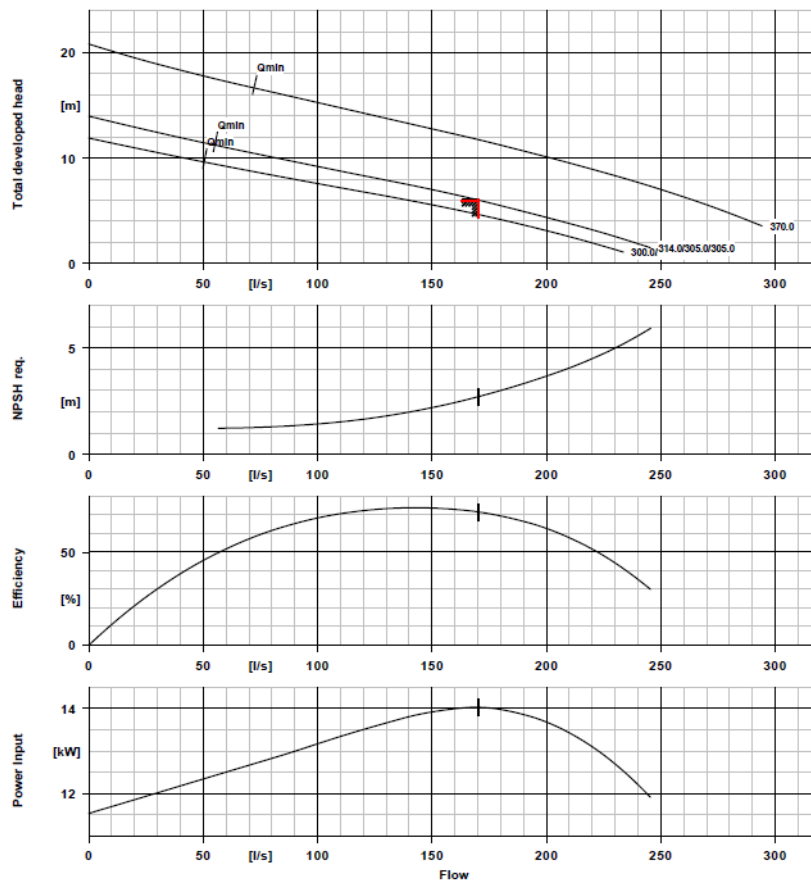


Figure 28: Pump curves at 400V and 50 Hz (Amarex impeller diameter: 305 mm) with the operating point: 6 m, 170 l/s, 71 %, 14 kW

Based on these information, the per unit basis introduced in section 2.2.1, can be computed in Table 13 for the Amarex pump. This pump was tested according to the procedure n°1 in section 2.1.3. In Figure 29, the installation of the pump is shown inside the tank.

Units	Basis
Time	$t_B = \frac{1}{\omega_B} = \frac{1}{2\pi f_B} = 3.18 \text{ ms}$
Power	$S_B = \frac{P_n}{PF} = \frac{18}{0.85} = 21.18 \text{ kVA}$
Voltage	$V_B = 400 \text{ V}$
Current	$I_B = \frac{S_B}{3V_B} = 17.65 \text{ A}$
Impedance	$Z_B = \frac{3V_B^2}{S_B} = 22.67 \Omega$
Flux	$\psi_B = V_B t_B = 1.27 \text{ Wb}$
Rotor speed	$\omega_{mB} = \frac{\omega_B}{p} = 1000 \text{ RPM}$
Torque	$T_B = \frac{S_B}{\omega_{mB}} = 202.22 \text{ Nm}$
Head	$H_B = H_p(Q = 0) = 14 \text{ m}$
Flow rate	$Q_B = \frac{S_B}{\rho g H_B} = 154.2 \text{ l/s}$

Table 13 : Basis used for the Amarex pump to pass in per unit system.



Figure 29: Amarex pump placed inside the tank

### 2.3.2 Pump 2: Flygt 3171.181 LT611

The main operating characteristics of the pump is listed in Table 14 and documented in 6.2. It is to note that some information is missing because it is not entered in the datasheet. The technical drawing of the pump is displayed in Figure 30. The pump curves provided by the datasheet is shown in Figure 31.

Flow rate	? l/s	Nominal voltage	400 V
Head	? m	Nominal frequency	50 Hz
Operating speed	965 RPM	Nominal electrical power	15 kW

Absorbed power	? kW	Nominal current	30 A
Efficiency	? %	Nominal efficiency	? %
Number of pair of poles	3	Nominal power factor	0.84

Table 14 : Operating characteristics of the 'Amarex KRT D 250 - 400/206UG-S' pump.

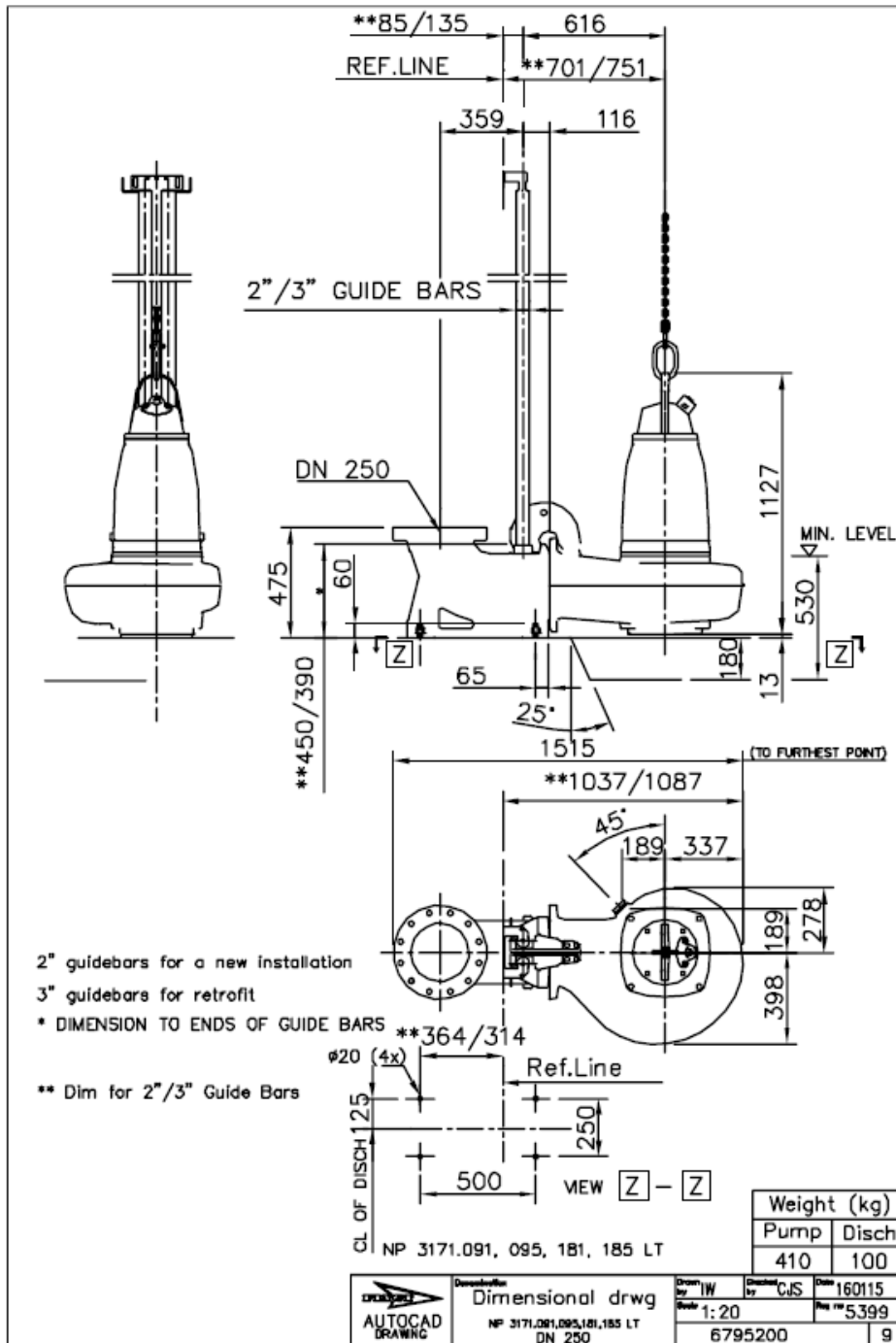


Figure 30: Technical drawing of the Flygt pump

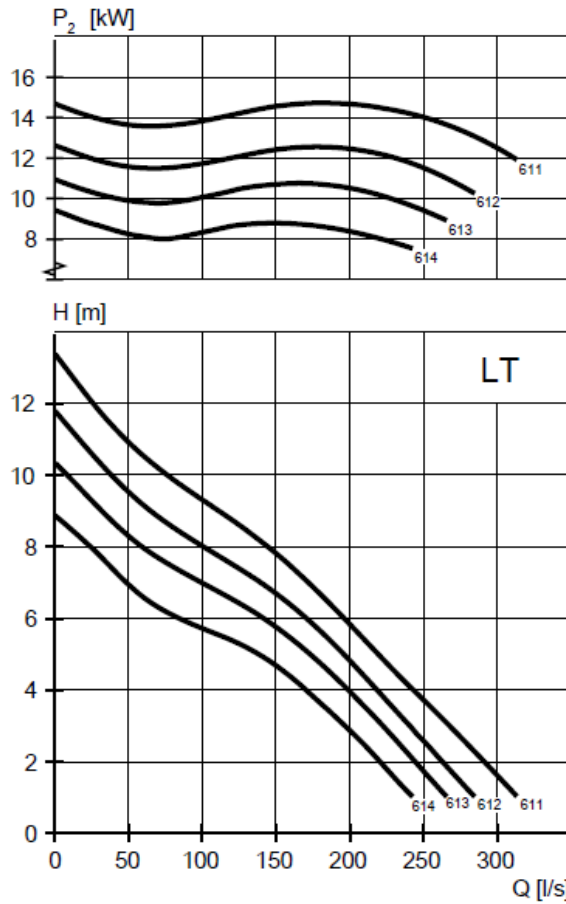


Figure 31: FLYGT pump curves at 400V and 50 Hz

Based on the above information, the per unit basis introduced in section 2.2.1, can be computed in Table 15 for the Flygt pump. This pump was tested according to the procedure n°1 in section 2.1.3. In Figure 32, the installation of the pump is shown inside the tank.

Units	Basis
Time	$t_B = \frac{1}{\omega_B} = \frac{1}{2\pi f_B} = 3.18 \text{ ms}$
Power	$S_B = \frac{P_n}{PF} = \frac{15}{0.84} = 17.86 \text{ kVA}$
Voltage	$V_B = 400 \text{ V}$
Current	$I_B = \frac{S_B}{3V_B} = 14.88 \text{ A}$
Impedance	$Z_B = \frac{3V_B^2}{S_B} = 26.88 \Omega$
Flux	$\psi_B = V_B t_B = 1.27 \text{ Wb}$
Rotor speed	$\omega_{mB} = \frac{\omega_B}{p} = 1000 \text{ RPM}$
Torque	$T_B = \frac{S_B}{\omega_{mB}} = 170.52 \text{ Nm}$
Head	$H_B = H_p(Q = 0) = 13.34 \text{ m}$
Flow rate	$Q_B = \frac{S_B}{\rho g H_B} = 136.4 \text{ l/s}$

Table 15 : Basis used for the Flygt pump to pass in per unit system.



Figure 32: Flygt pump placed inside the tank

## 3 Results

### 3.1 Experimental observation

#### 3.1.1 Pump 1: Amarex KRTK 250 - 400/206UG-S

The 51 measuring points ( $N_p = 51$ ) obtained during the test of the Amarex pump is drawn in Figure 33. As seen, the head-(flow rate) curve with a 50 Hz motor excitation, is quite near from the datasheet displayed in dashed line. The difference could be due to mainly two aspects: the neglected losses in pipes from the pump discharge to the pipe P20 and maybe in a least sense to the storage of the pump outside during several years. Regarding the total efficiency, as displayed in the datasheet, the same curve seems to apply whatever the size of the impeller which does not make sense. Besides, the efficiency drawn in Figure 28 is not well defined. There is no information to know whether it includes the motor efficiency. One has assumed it includes it and the curve gives the total efficiency of the motor and pump together. The efficiencies provided by experimental data and by the datasheet are really spaced and no explanation has been found for the moment.

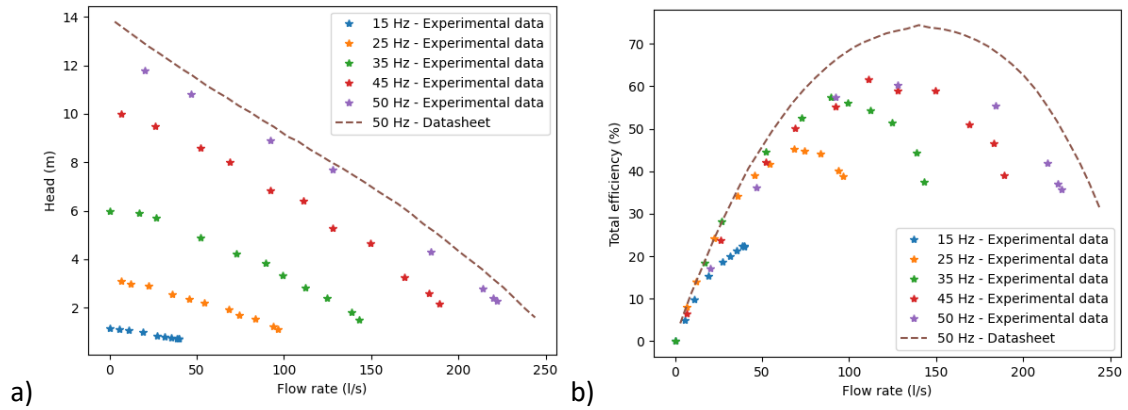


Figure 33: Experimental results compared to datasheet for the Amarex pump

The link between experimental data and the pump operation toolkit is made in section 3.2. It passes by the identification of the pump parameters that suits the best the experimental data. To find these coefficients, the calibration process explained in section 2.2.3 is performed.

### 3.1.2 Pump 2: Flygt 3171.181 LT611

In this section, the results of the test bench are displayed without any computational modelling. Yet, before explaining the results, the datasheet of the pump is a bit analysed. The overall efficiency is not represented in the datasheet. Nevertheless, it could be obtained by computation using the formula:  $\rho g \tilde{Q} \tilde{H} / \tilde{P}_e$  where the flow rate and the head are given by the pump curve and the electric power is obtained. The resulting efficiency is displayed in Figure 34. The overall maximum efficiency for the pump is of about 80%.

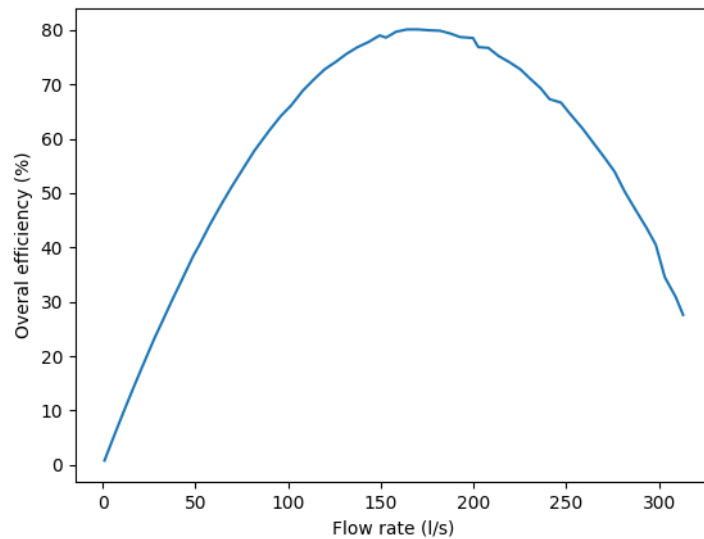


Figure 34: Overall pump efficiency computed based on the datasheet for the Flygt pump at nominal frequency 50 Hz

The 51 measuring points ( $N_p = 51$ ) obtained during the test of the Flygt pump is drawn in Figure 35. As seen, the head-(flow rate) curve with a 50 Hz motor excitation, is quite near from the datasheet displayed in dashed line. The difference could be due to the neglected losses in pipes from the pump discharge to the pipe P20. Besides, the efficiency drawn in Figure 34 is not well defined. There is no information to know whether it includes the motor efficiency. Indeed, the power communicated in the datasheet may either be the power consumption of the motor or the power generated by the motor and transferred to the pump wheel. One has assumed it is the power consumption and the curve gives the total efficiency of the motor and pump together. The efficiencies provided by

experimental data and by the datasheet are really spaced and no explanation has been found for the moment.

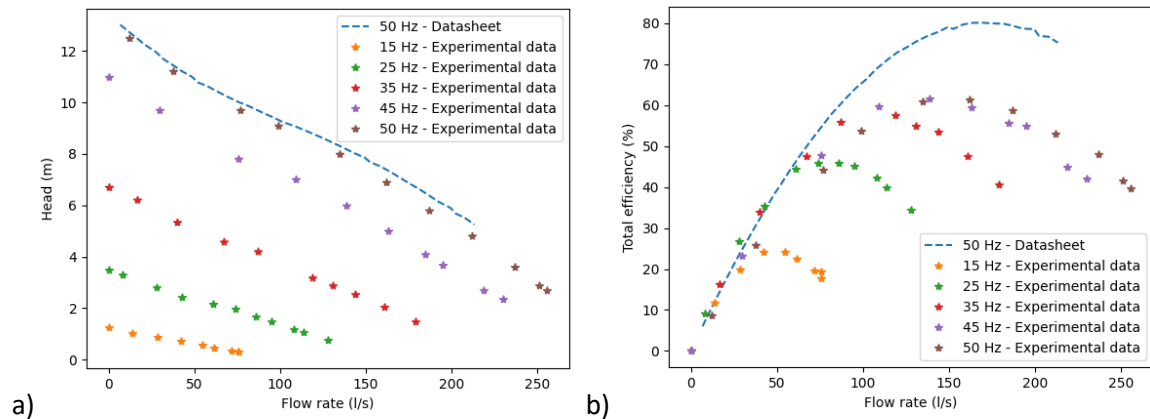


Figure 35: Experimental results compared to datasheet for the Flygt pump

## 3.2 Computational results

### 3.2.1 Pump1: Amarex KRTK 250 - 400/206UG-S

The test of this pump provide data recorded about the flow rates, the heads, the power consumptions for several motor excitations. The calibration procedure is then applied with the bench results to provide parameters to the numerical model of pump. The parameters obtained are given in Table 16. The root mean square differences between computations and measurements are in average 6 %, 5 % and 7 % for the flowrate, the electric power and the total efficiency, with a standard deviation of 6 %, 5 %, 7 %.

$a_{app}$	$b_{app}$	$c_{app}$	$d_{app}$	$e_{app}$	$f_{app}$
-0.1324	-0.3579	1.1039	-0.3481	0.6389	0.6660
$R_s$	$R_r$	$L_{SS}$	$L_{SR}$	$L_{rr}$	$A_{fr}$
0.12523	0.05905	2.14154	2.05823	2.14518	0.14887
$a$	$b$	$c$	$d$	$e$	$f$
-0.15581	-0.29619	0.96051	-0.17884	0.30918	0.39379

Table 16: Numerical model parameters identified in the calibration procedure with  $c_Q = 0.5$

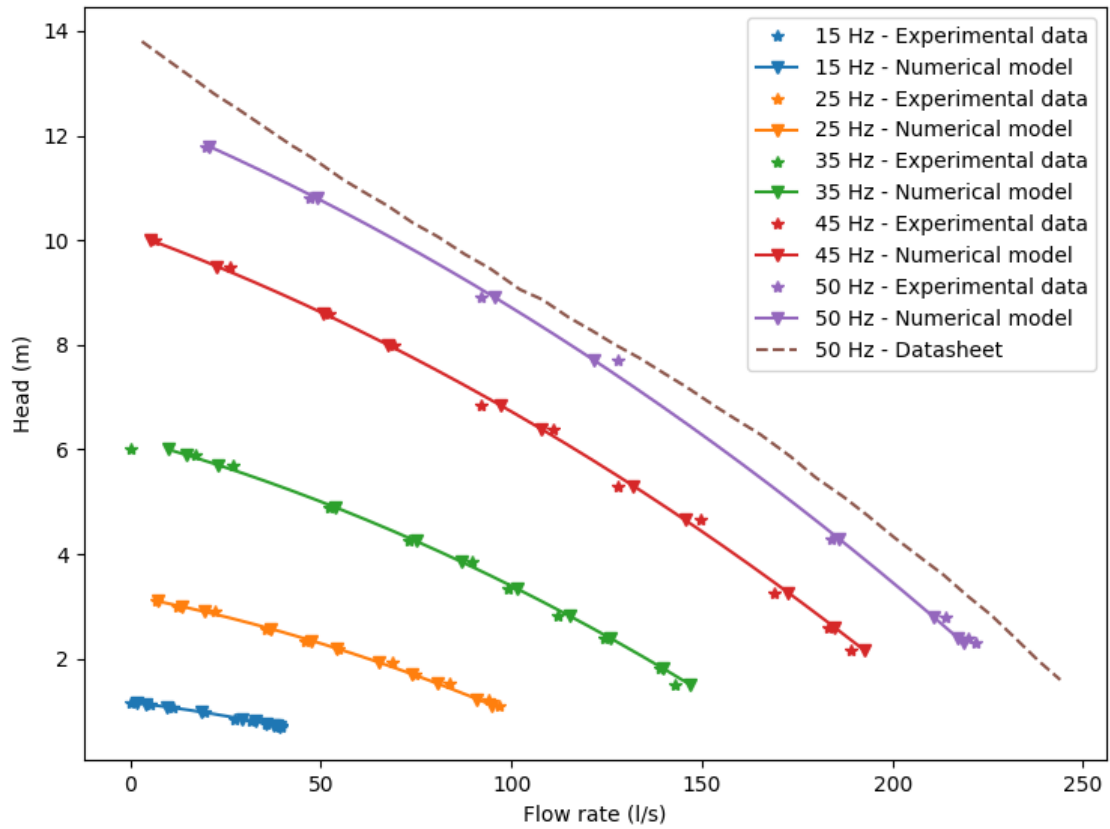


Figure 36: Comparison between pump curves provided by the bench measurements (star) and the numerical model (triangle)

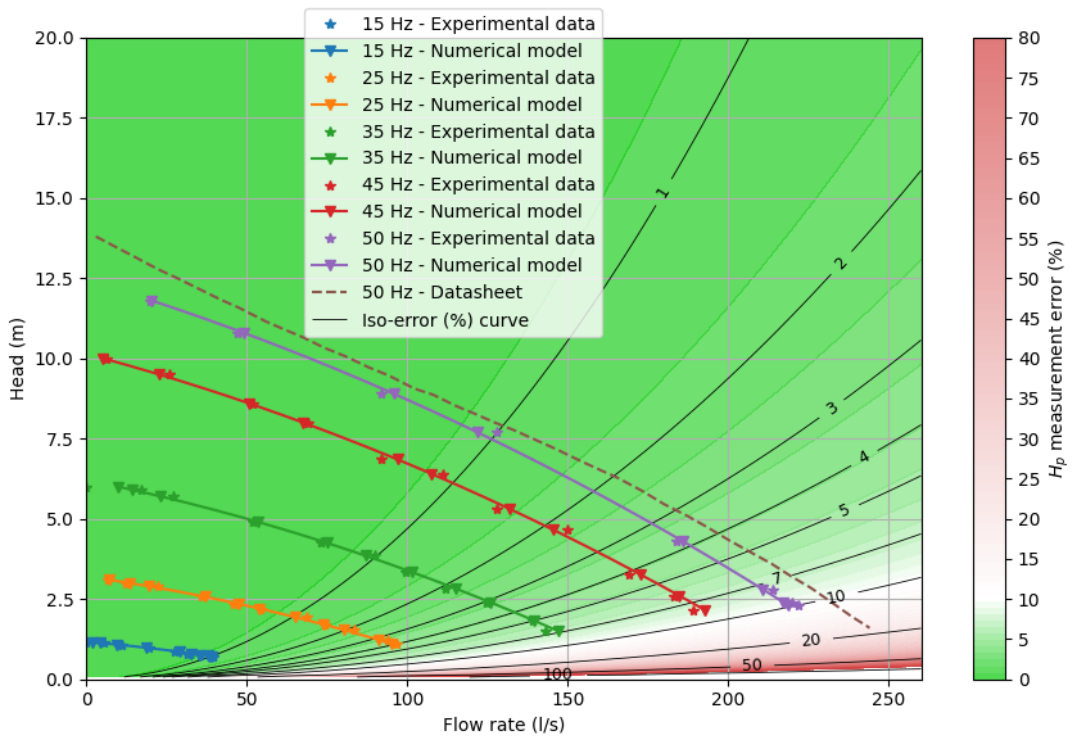


Figure 37:

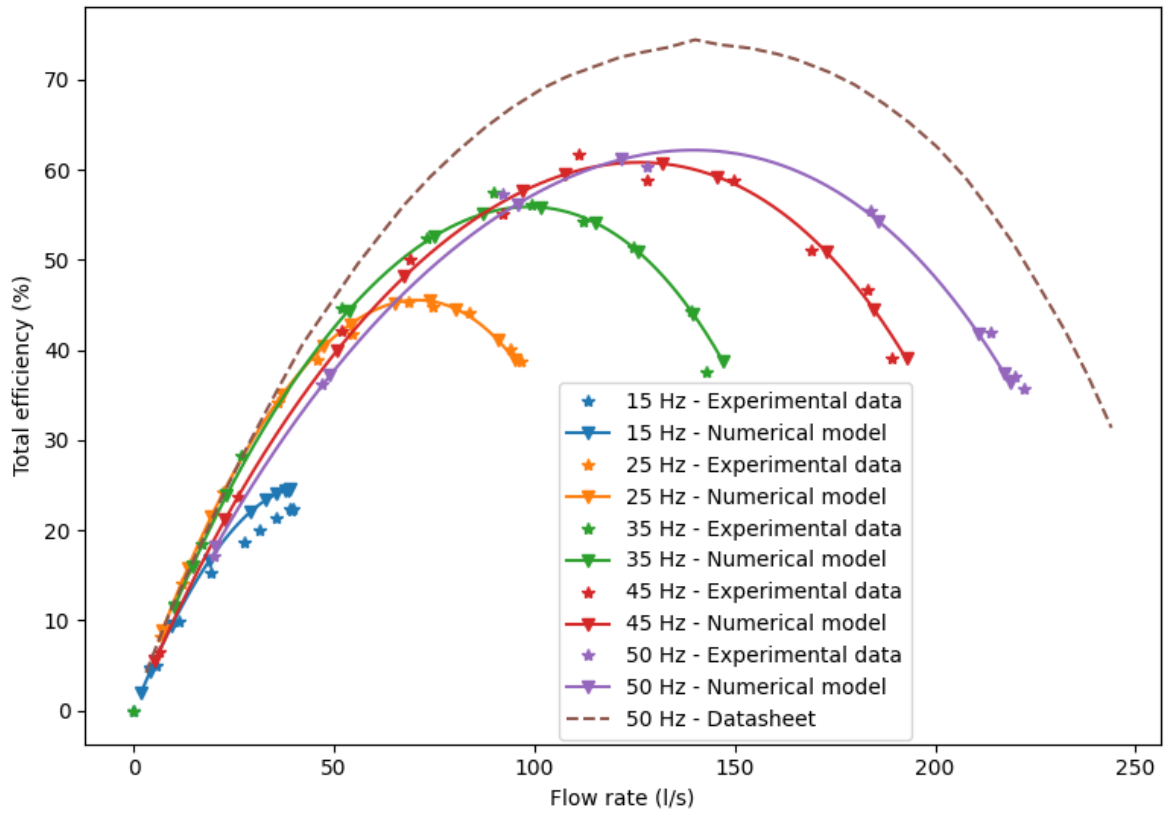


Figure 38: Comparison between total efficiency curves provided by the bench measurements (star) and the numerical model (triangle)

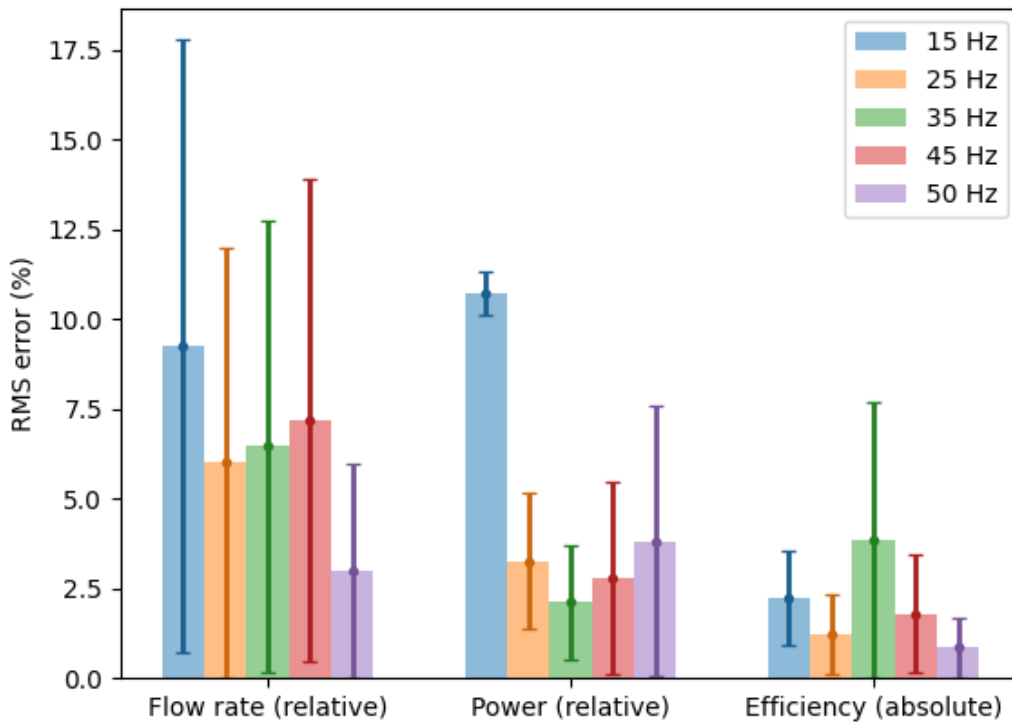


Figure 39: Distribution of the RMS error and standard deviation for flow rate, power consumption and total efficiency between numerical model and experimental results

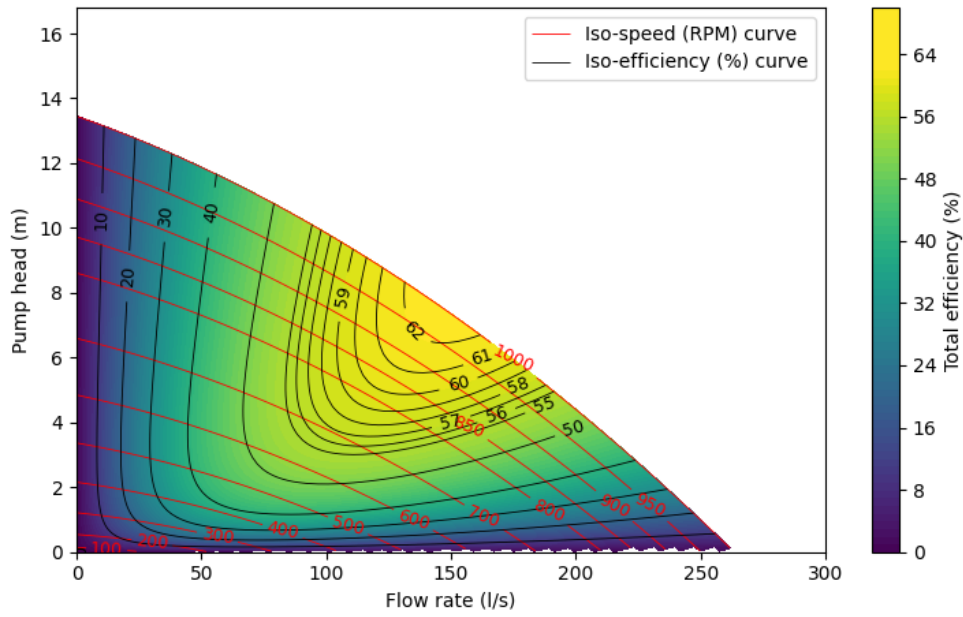


Figure 40: Efficiency map of the motor-pump assembly (Attention, it does not take into account the hydraulic efficiency of the suction/discharge system) with BEP (6.85 m; 139.27 l/s)

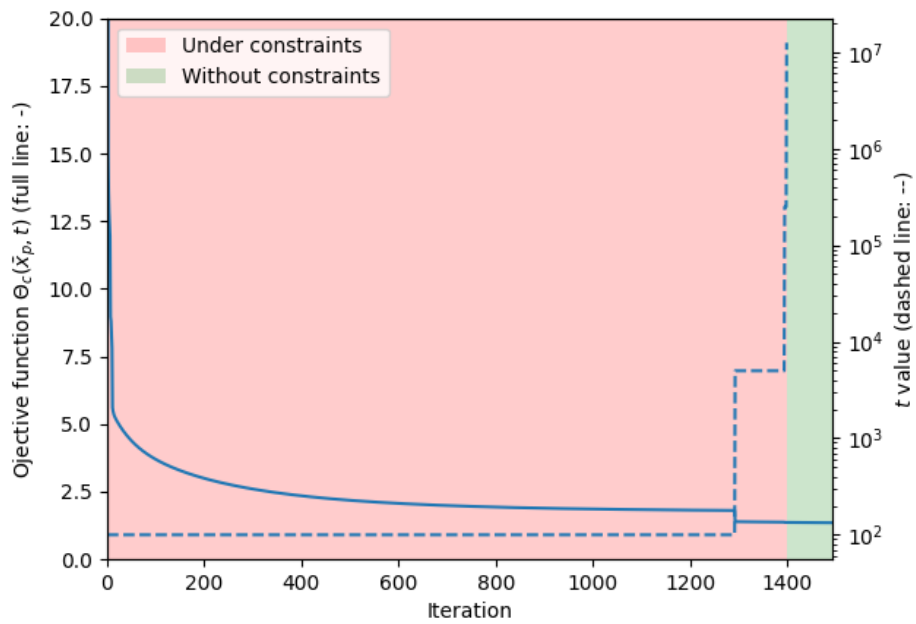


Figure 41: Objective function (full line) and value of t (dashed line) during the calibration

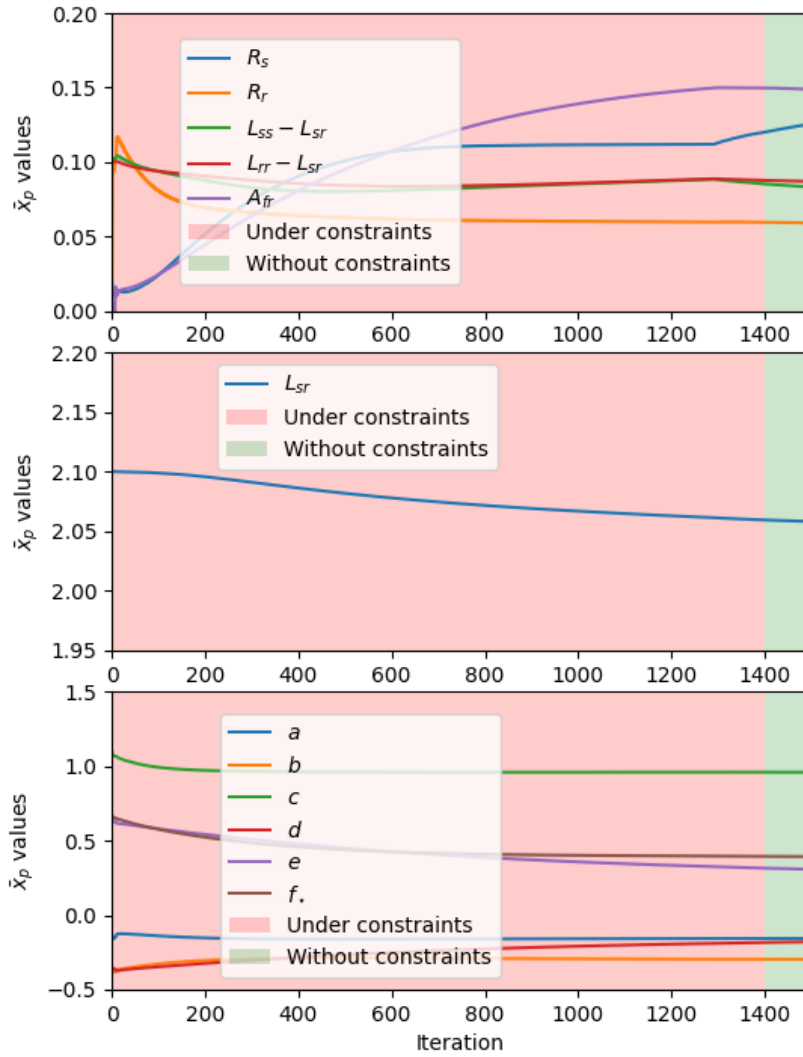


Figure 42: the 11 parameters during the calibration

**Influence of the coefficient  $c_Q$ :**

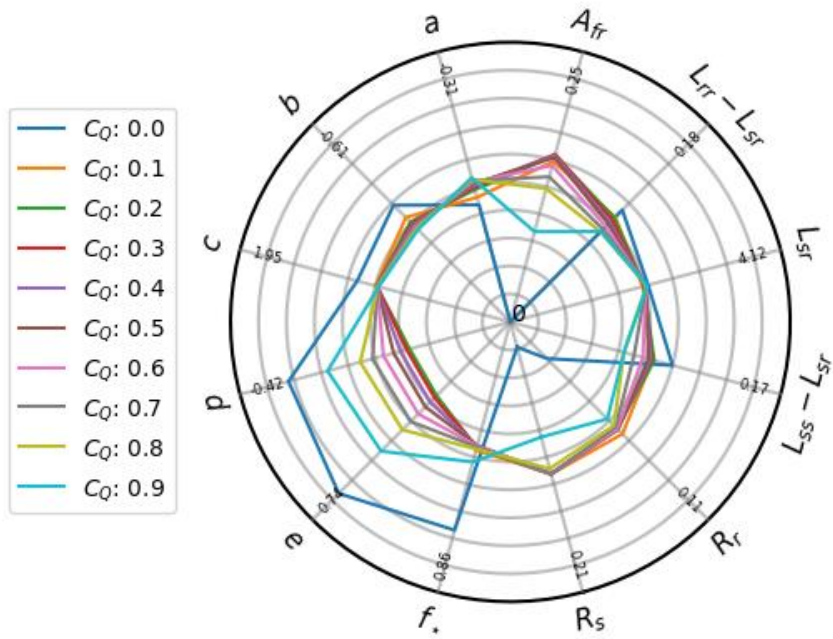


Figure 43: Calibrated coefficients obtained for several values of  $c_Q$

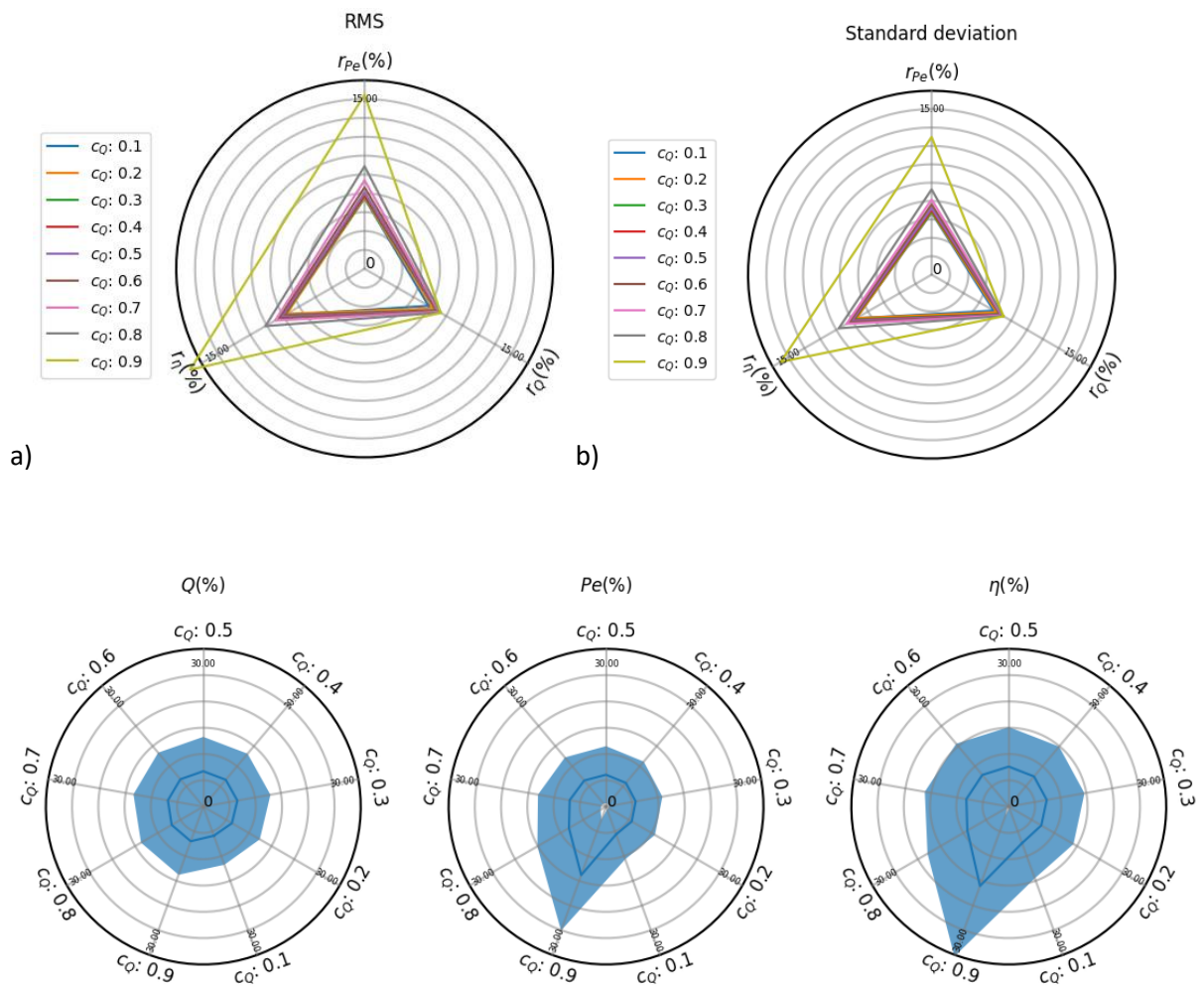
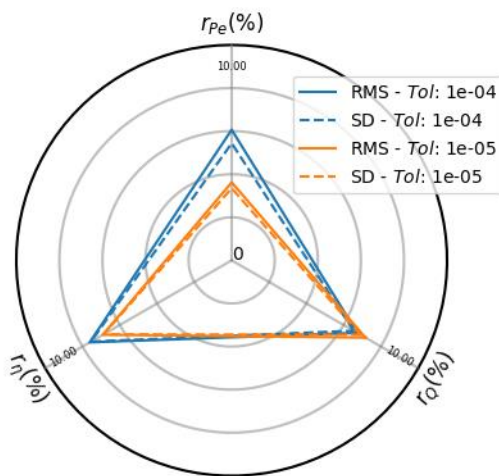
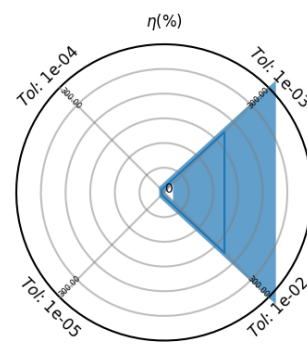
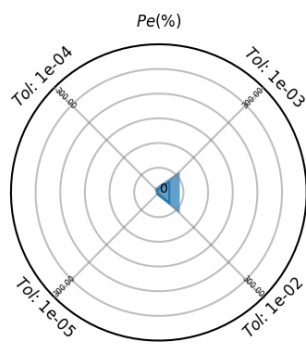
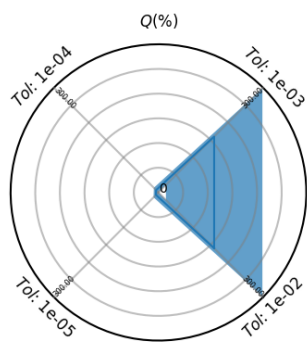
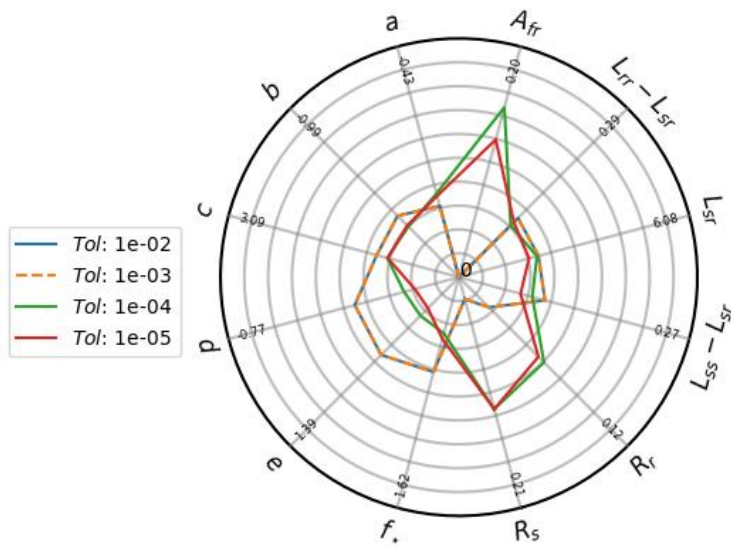
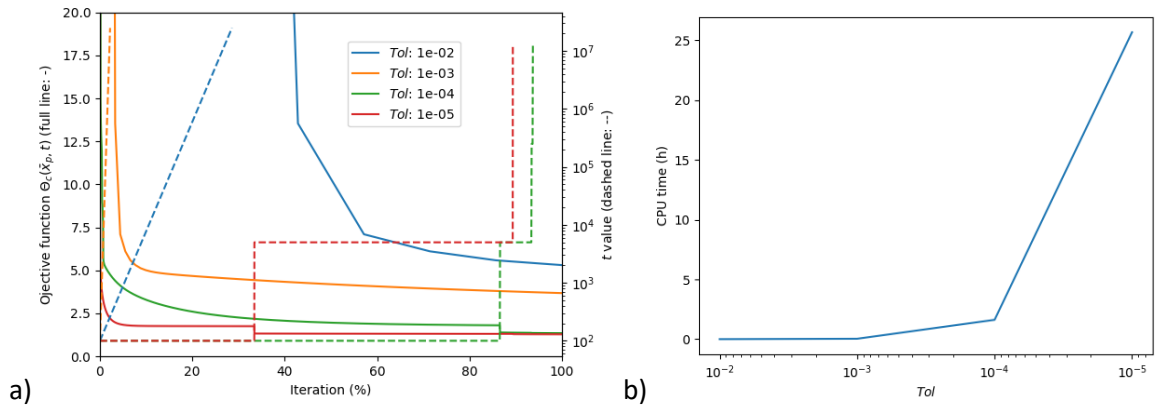


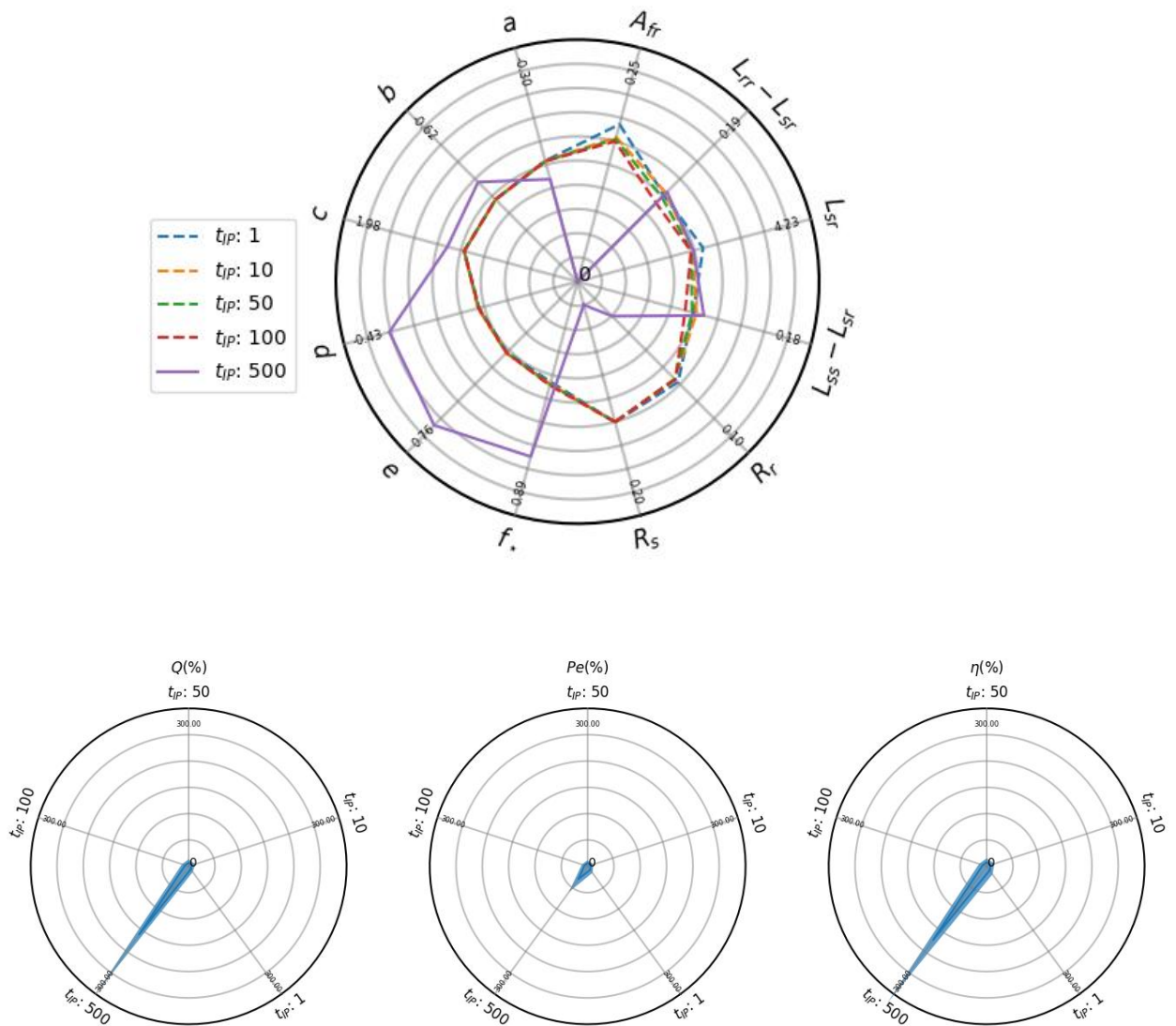
Figure 44: Influence of the coefficient  $c_Q$  in the objective function on the identification of the coefficient of the mathematical model.

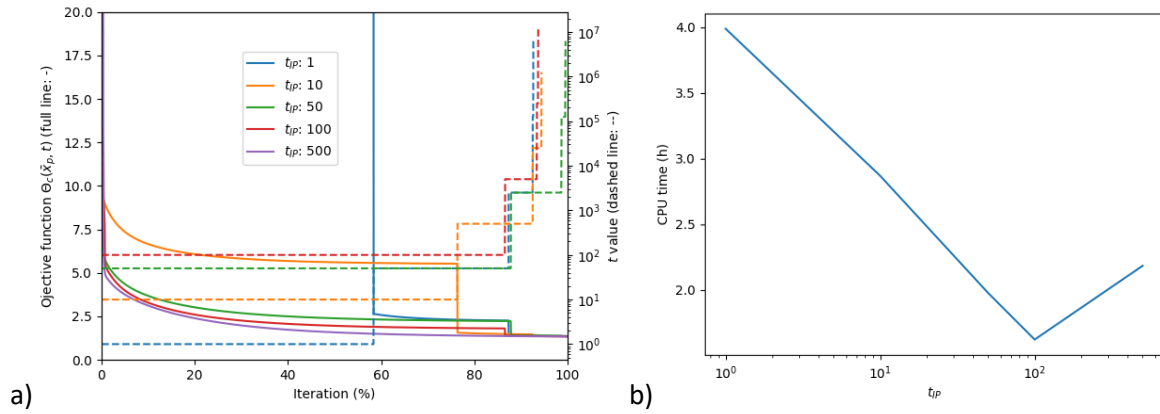
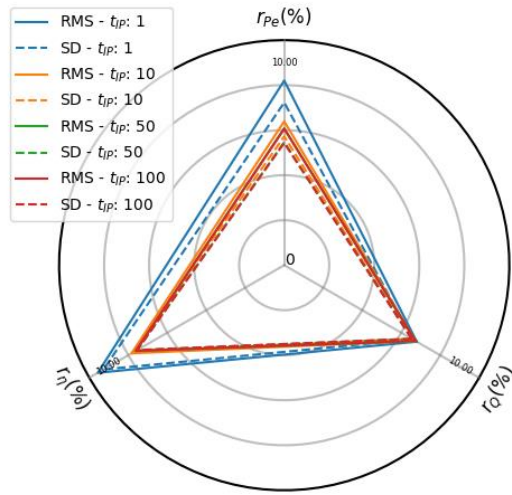
Variation of the coefficient  $Tol$ :



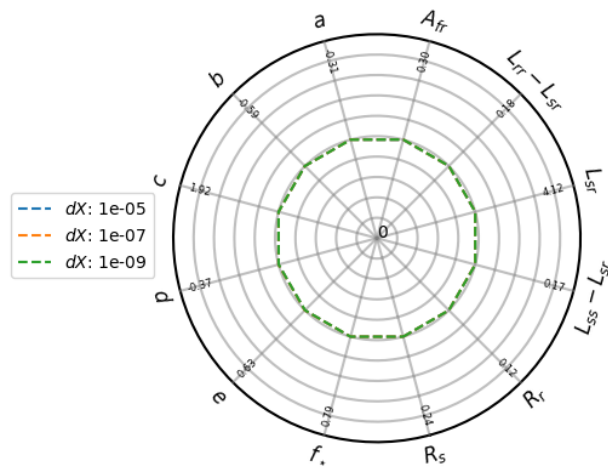


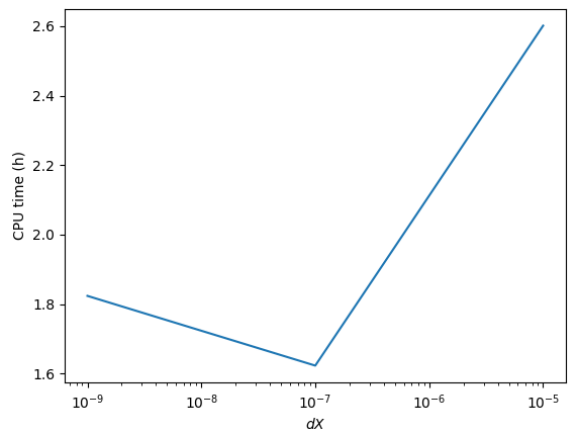
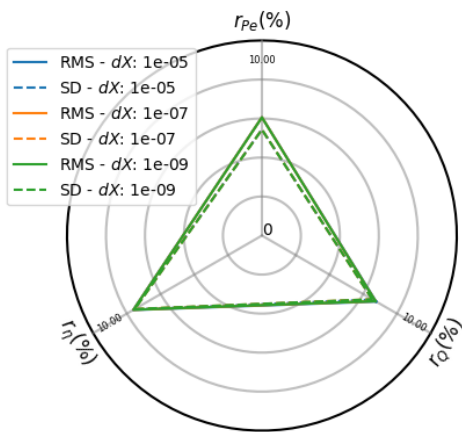
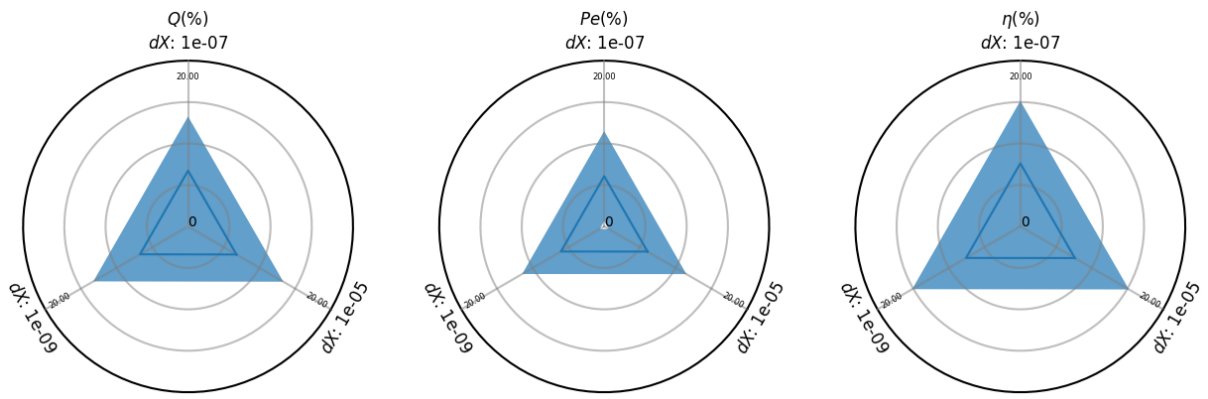
Variation of coefficient  $t_{IP}$ :





Variation of coefficient  $dX$ :

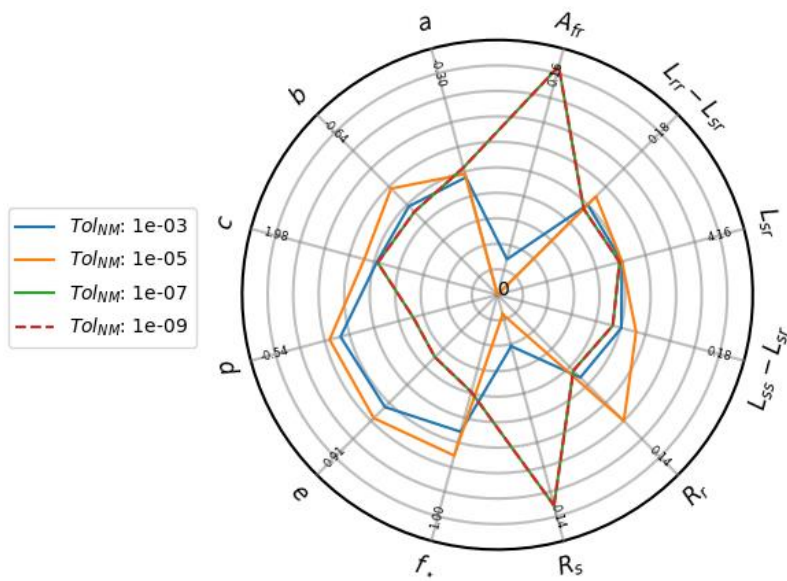


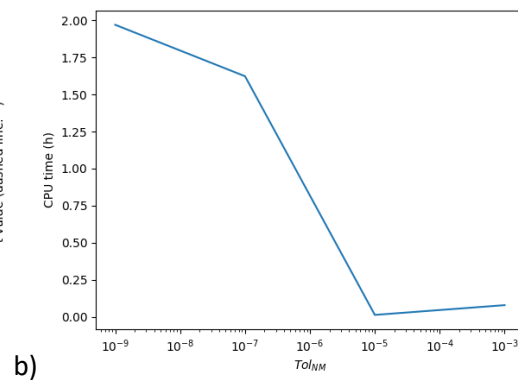
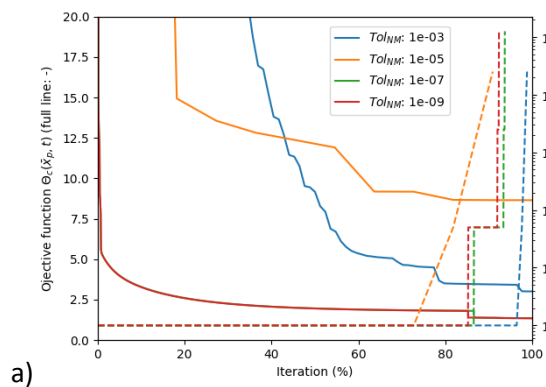
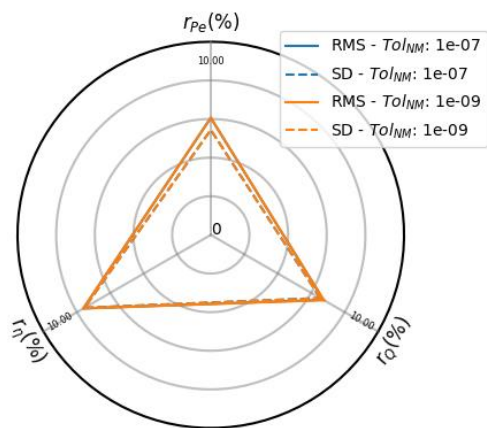
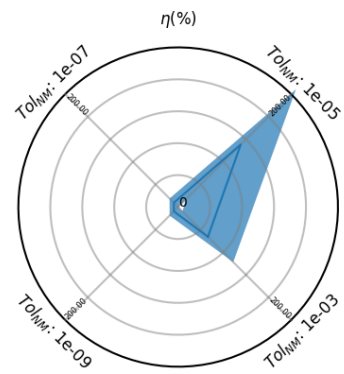
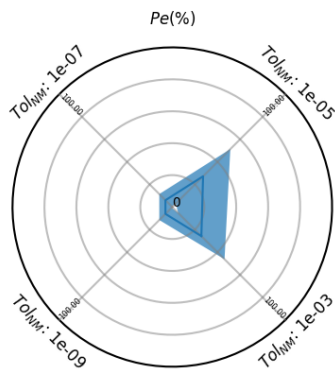
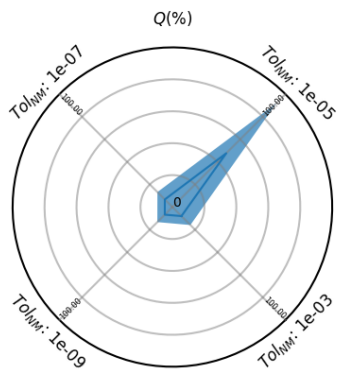


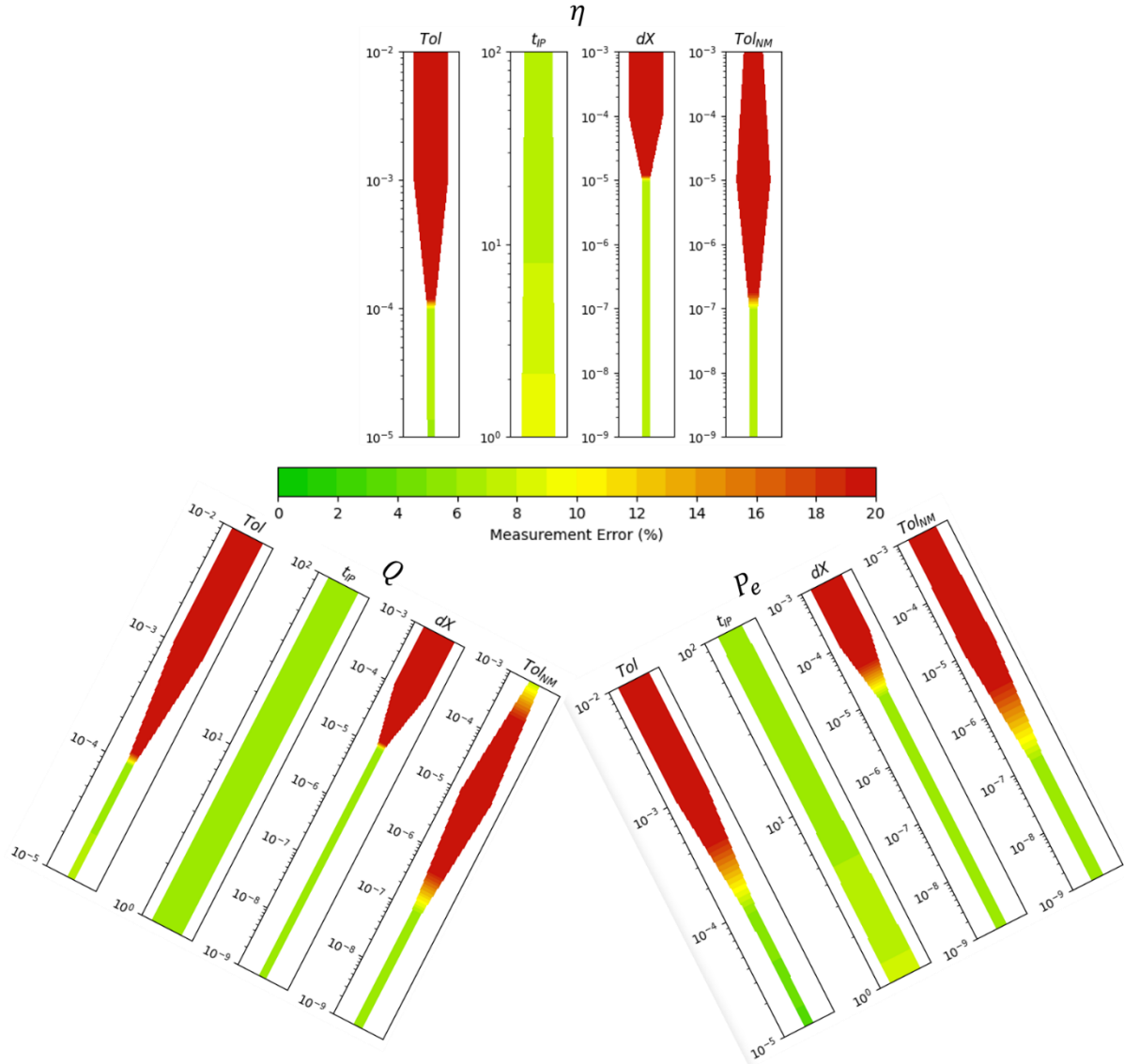
a)

b)

Variation of coefficient  $Tol_{NM}$ :







### 3.2.2 Pump 2: Flygt 3171.181 LT611

The test of this pump provide data recorded about the flow rates, the heads, the power consumptions for several motor excitations. The calibration procedure is then applied with the bench results to provide parameters to the numerical model of pump. The parameters obtained are given in Table 16. The root mean square differences between computations and measurements are in average 9 %, 3 % and 2 % for the flowrate, the electric power and the total efficiency, with a standard deviation of 8 %, 3 %, 2 %.

$a_{app}$	$b_{app}$	$c_{app}$	$d_{app}$	$e_{app}$	$f_{app}$
-0.01506	-0.42264	1.21246	-0.32599	0.90402	0.70998
$R_s$	$R_r$	$L_{ss}$	$L_{sr}$	$L_{rr}$	$A_{fr}$
0.10695	0.04017	2.16262	2.08488	2.16595	0.19401
$a$	$b$	$c$	$d$	$e$	$f$
-0.02201	-0.37543	1.05563	-0.02800	0.08413	0.66783

Table 17: Numerical model parameters identified in the calibration procedure with  $c_Q = 0.5$

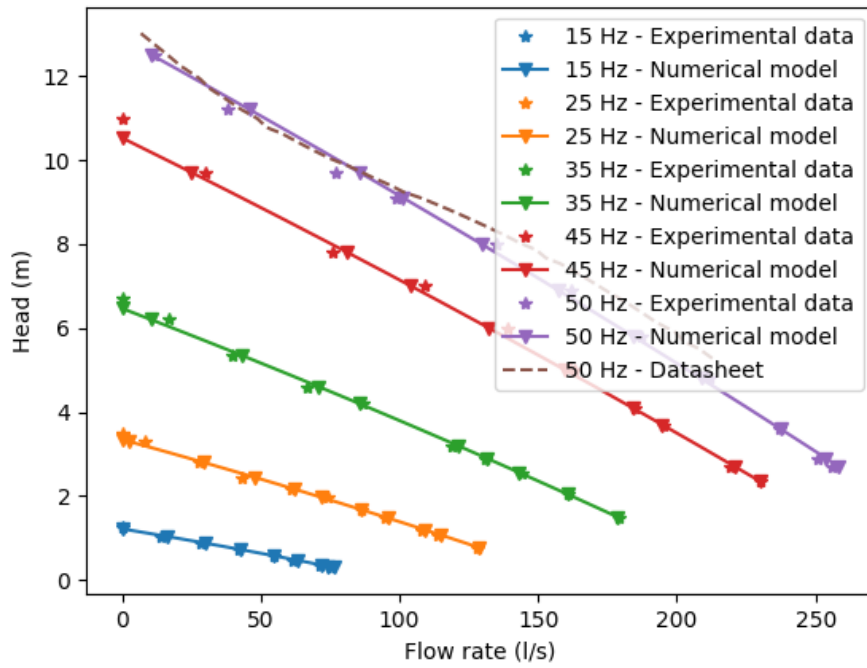


Figure 45: Comparison between pump curves provided by the bench measurements (star) and the numerical model (triangle)

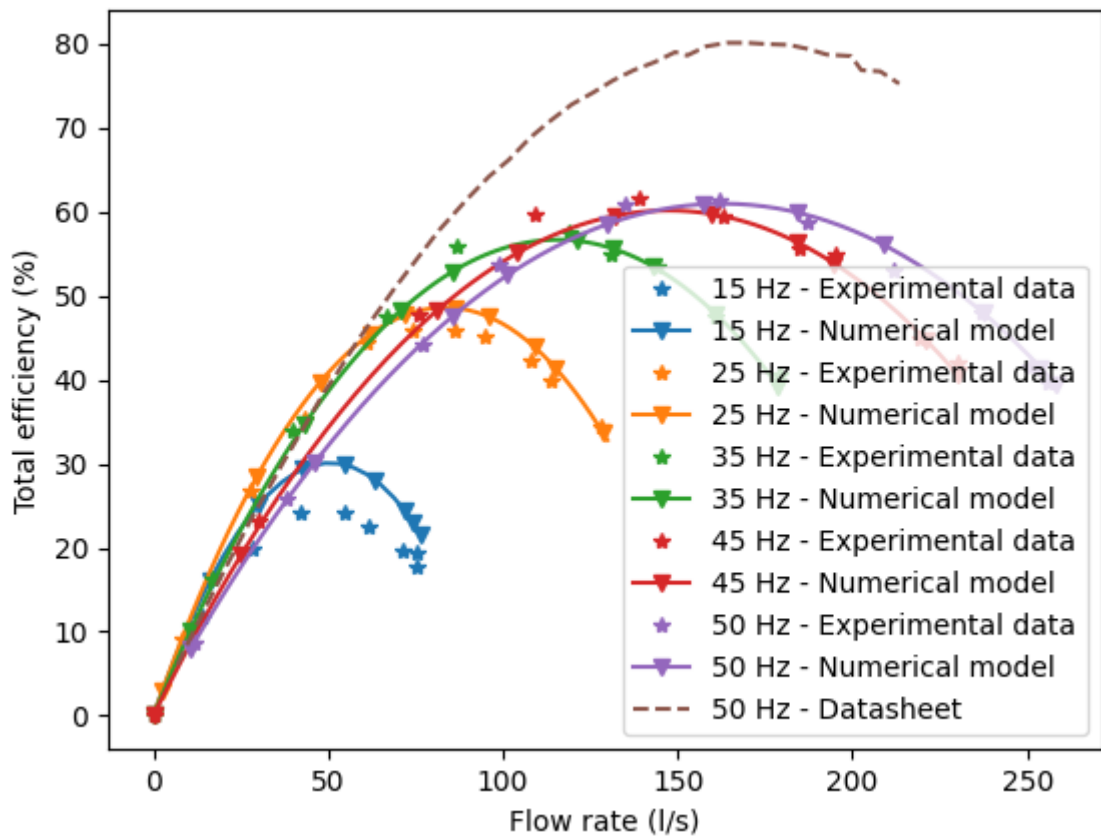


Figure 46: Comparison between total efficiency curves provided by the bench measurements (star) and the numerical model (triangle)

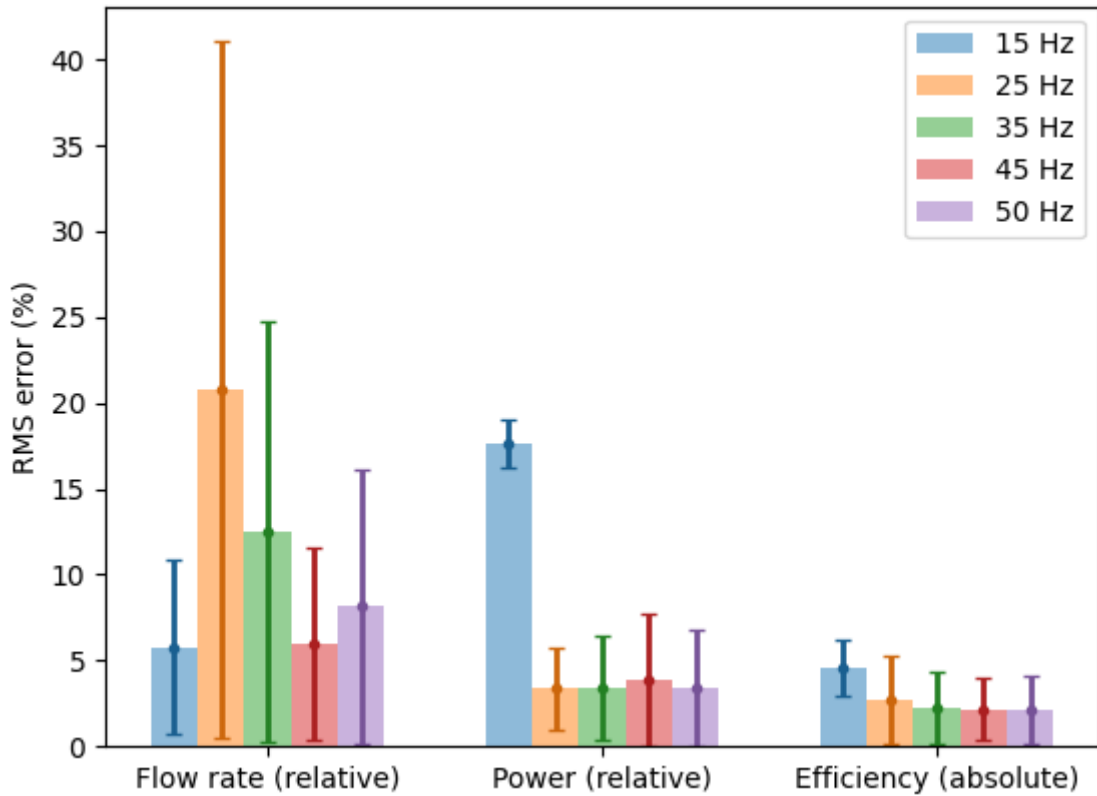


Figure 47: Distribution of the RMS error and standard deviation for flow rate, power consumption and total efficiency between numerical model and experimental results

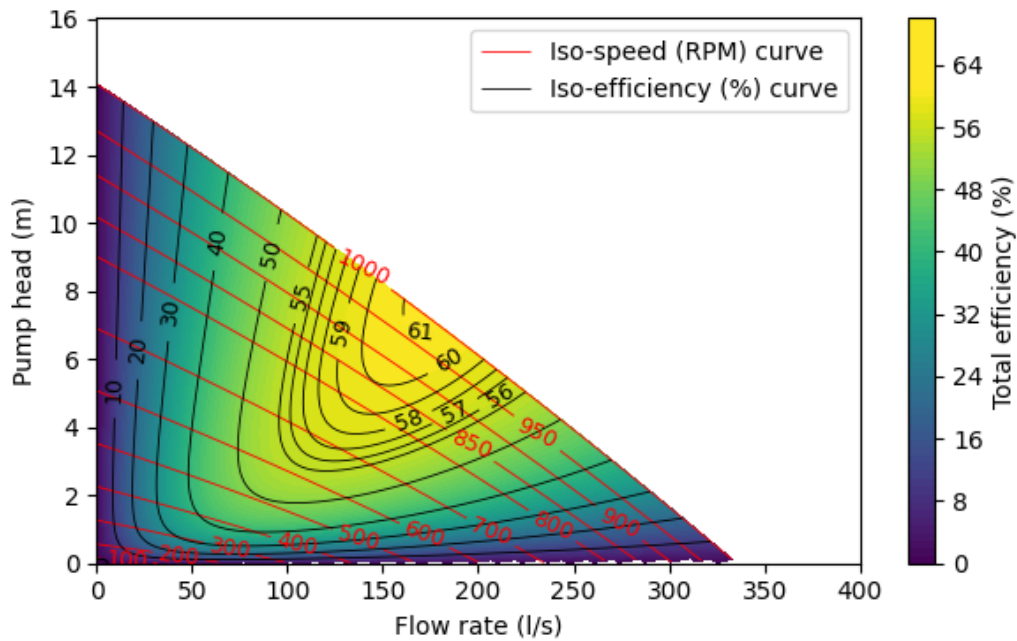


Figure 48: Efficiency map of the motor-pump assembly (Attention, it does not take into account the hydraulic efficiency of the suction/discharge system) with a computed BEP (6.678 m; 162.77 l/s) at constant frequency 50 Hz

## 4 Conclusions

To conclude, the ...

## 5 References

- [1] Engineering ToolBox. Centrifugal Pumps - Speed Torque Curve, 2008, [https://www.engineeringtoolbox.com/pumps-speed-torque-d\\_1114.html](https://www.engineeringtoolbox.com/pumps-speed-torque-d_1114.html);
- [2] Fitzgerald E., Charles Kingsley. Jr., Stephen D. Umans. Electric Machinery, sixth edition. Book, pp. 664-667, 2003;
- [3] Guedelha N., Silvio T., and Daniele P. Identification of Motor Parameters on Coupled Joints. ArXiv: 1906.05070 [Cs], 2019, <https://arxiv.org/pdf/1906.05070.pdf>;
- [4] Hardy J., et al. Experimental Test Bench for Performance-Assessment of Large Submersible and Dry-Action Pumps Used in Waterways. Publ. Inst. Geophys. Pol. Acad. Sci. Geophys. Data Bases Process. Instrum. 434, pp. 101–103, 2021.
- [5] Idelcik I.E., Memento des pertes de charge, Coefficients de pertes de charge singulières et de pertes de charge par frottement. Eyrolles, traduit du russe par Mme M. Meury, tirage de 1979.
- [6] Isoil industria. Data sheet MV110 CE. ISOMAG, The friendly magmeter, 1-7-2.
- [7] Janevska G. Mathematical Modeling of Pump System. EIC the 2<sup>nd</sup> Electronic International Interdisciplinary Conference, Zilina, Czech Republic, 2013, [https://www.researchgate.net/publication/283348821\\_Mathematical\\_Modeling\\_of\\_Pump\\_System](https://www.researchgate.net/publication/283348821_Mathematical_Modeling_of_Pump_System);
- [8] KSB. KRTK 250-400/206UG-S. Data sheet 4002096785, 2014 ; [A ajouter en annexe]
- [9] Lathrop D.P., Fineberg J. and Swinney H.L. Turbulent flow between concentric rotating cylinders at large Reynolds number. Physical Review Letters, Vol. 68, No. 10, pp. 1515-1518, 1992, <https://journals.aps.org/prl/pdf/10.1103/PhysRevLett.68.1515>.
- [10] Leonhard W. Control of Electrical Drives, third edition. Book, pp. 163-211, 2001;
- [11] MathWorks. Centrifugal pump. Documentation: Simscape, Fluids, Hydraulics (isothermal), Pumps and Motors; Description: Parameterizing the Pump by Approximating Polynomial; R2021b, <https://www.mathworks.com/help/phymod/hydro/ref/centrifugalpump.html>.
- [12] Osmanaj S., Simnica Aliu K., Limani M., Kabashi Q. The sensitivity of the hoist system in crane applications from speed control methods at induction motors. Elektrotechnik & Informationstechnik, Fig. 3, 2018, <https://doi.org/10.1007/s00502-018-0606-7>.
- [13] Stewart M. 3 - Centrifugal pumps. Surface Production Operations, Gulf Professional Publishing, section 3.6.2, pp. 120-124, ISBN 9780128098950, 2019, <https://doi.org/10.1016/B978-0-12-809895-0.00003-X>.
- [14] Sulzer-Pumpen. Special Data for Planning Centrifugal Pump Installations. In: Sulzer-Pumpen (eds.), Centrifugal pump handbook, Elsevier, Switzerland, 91-97, 2010;
- [15] Tozen, Equivalent pipe length/friction head (rubber flexible expansion joints, rubber flexible joints and fluoro carbon polymer flexible joints). Frequently-asked questions, [https://www.tozen.co.jp/en/support/faq\\_technology/](https://www.tozen.co.jp/en/support/faq_technology/) (consulted on the 11<sup>th</sup> of February 2022).
- [16] U.S Department of Energy, A.M.O., 2012. Adjustable Speed Drive Part-Load Efficiency.

- [17] Van Cutsem T. Power systems dynamics, control and stability, Dynamics of the induction machine, course, sl.9, 2019, <https://thierryvancutsem.github.io/home/courses.html>;
- [18] Van Cutsem T., Vournas C. Voltage Stability of Electric Power System. New York, Springer, pp. 100-113, 1998.
- [19] Vasudevan K., G. Sridhara Rao, P. Sasidhara Rao. Electrical Machines II, Part 8, Speed control of Induction Machines. Indian Institute of Technology Madras, pp. 30-41;

## 6 Appendices

### 6.1 Appendix 1: pump equations

The pump equations are derived from [7], [13] and [11]. The head can be expressed as a 2<sup>nd</sup> degree polynomial of the flow rate for a given constant rotation speed:

$$H_p = c_0 + c_1 Q + c_2 Q^2$$

with  $c_0, c_1, c_2$  constant coefficients.

The affinity laws presented in [13] allow to compute the pump head as well as the flow rate at another rotation speed based on a reference:

$$\frac{H_{p,new}}{H_{ref}} = \left( \frac{\omega_{r,new}}{\omega_{r,ref}} \right)^2$$
$$\frac{Q_{new}}{Q_{ref}} = \frac{\omega_{r,new}}{\omega_{r,ref}}$$

The pump head equation at the reference rotation speed can be written as:

$$H'_p = c'_0 + c'_1 Q' + c'_2 Q'^2$$

The reference statement can be written depending on the head and the flow rate corresponding to a different rotation speed  $\omega_r$ :

$$H_p \left( \frac{\omega'_r}{\omega_r} \right)^2 = c'_0 + c'_1 Q \frac{\omega'_r}{\omega_r} + c'_2 Q^2 \left( \frac{\omega'_r}{\omega_r} \right)^2$$
$$\Rightarrow H_p = \frac{c'_0}{\omega_r'^2} \omega_r^2 + \frac{c'_1}{\omega_r'} Q \omega_r + c'_2 Q^2$$
$$\Rightarrow H_p = c \omega_r^2 + b Q \omega_r + a Q^2$$

For the pump torque expression, it is given in [11] as:

$$T_p = k_0 \omega_r^2 + (T_0 + k_p H_p)$$

Where  $T_0 = 0$ , we consider that no constant term is present in the shaft bearing friction. It leads to finally:

$$T_p = f_* \omega_r^2 + e Q \omega_r + d Q^2$$

As seen, the torque is a second degree polynomial in the rotation speed what remains in agreement with the content of [18] and [1].

### 6.2 Appendix 2: FLYGT datasheet

In this appendix, the detailed datasheet relative to the pump n°2 is included from the main datasheet provided by the FLYGT company.

## 3 Pompe N, moteur standard

### 3.1 Descriptif du produit



#### Utilisation

Pompe submersible pour le pompage à haut rendement d'eau propre, d'eau de surface et d'eau usée contenant des solides ou des matières à fibres longues. La pompe est conçue pour assurer un haut rendement constant. Pour les fluides abrasifs, le matériau Hard-Iron™ est obligatoire. La roue N en acier inoxydable est proposée en option.

#### Désignation

Type	Version non antidéflagrante	Version antidéflagrante	Classe de pression	Types d'installation
Fonte grise	3171.181	3171.091	LT – basse pression MT – moyenne pression HT – haute pression SH – super haute pression	P, S, T, Z
Hard-Iron™	3171.185	3171.095	LT – basse pression MT – moyenne pression HT – haute pression SH – super haute pression	P, S, T, Z
Fabrication en acier inoxydable	3171.660	3171.670	MT – moyenne pression	P, S

La pompe peut s'utiliser dans les installations suivantes :

- P Installation semi-permanente en puisard avec la pompe montée sur deux barres de guidage. Le raccordement au refoulement est automatique.
- S Installation semi-permanente portable, en puisard avec raccord pour tuyau ou bride de raccordement à une canalisation de refoulement.
- T Installation verticale permanente, à sec avec raccordement par bride aux canalisations d'aspiration et de refoulement.
- Z Installation verticale permanente, à sec avec raccordement par bride aux canalisations d'aspiration et de refoulement.

#### Limites d'application

Caractéristique	Description
Température de liquide	Maximum 40°C (104°F)

Caractéristique	Description
Température du liquide, version pour eau chaude	Maximum 70°C (158°F)
Profondeur d'immersion	Maximum 20 m (65 pi)
pH du liquide pompé	5,5-14
Densité du liquide	Maximum 1100 kg/m <sup>3</sup>

#### Caractéristiques du moteur

Caractéristique	Description
Type de moteur	Moteur cage à induction
Fréquence	50 Hz
Alimentation	Triphasé
Méthode de démarrage	<ul style="list-style-type: none"> <li>• Mode direct (DOL)</li> <li>• Étoile-triangle</li> <li>• Variateur (VFD)</li> </ul>
Nombre de démarrages par heure	Maximum 30
Conformité aux codes	CEI 60034-1
Variation de tension	<ul style="list-style-type: none"> <li>• Régime continu : maximum <math>\pm 5\%</math></li> <li>• Fonctionnement intermittent : maximum <math>\pm 10\%</math></li> </ul>
Déséquilibre de tension entre les phases	Maximum 2 %
Classe d'isolement du stator	H (180°C, 356°F)

#### Câbles

Application	Type
Démarrage direct en ligne ou démarrage étoile/triangle avec deux câbles	SUBCAB® Flygt - câble d'alimentation de moteur renforcé à 4 conducteurs et deux paires torsadées de conducteurs auxiliaires. Isolation des conducteurs résistant à 90°C, autorisant des courants supérieurs. Résistance mécanique supérieure, forte résistance à l'abrasion et à l'usure. Résistance aux produits chimiques en pH 3-10 et à l'ozone, à l'huile et à la flamme. Utilisable jusqu'à une température d'eau de 70°C. Câbles < 10 mm <sup>2</sup> avec conducteurs auxiliaires non blindés.
Démarrage étoile/triangle	SUBCAB® Flygt - câble d'alimentation de moteur renforcé à 7 conducteurs et deux paires torsadées de conducteurs auxiliaires. Isolation des conducteurs résistant à 90°C, autorisant des courants supérieurs. Résistance mécanique supérieure, forte résistance à l'abrasion et à l'usure. Résistance aux produits chimiques en pH 3-10 et à l'ozone, à l'huile et à la flamme. Utilisable jusqu'à une température d'eau de 70°C. Câbles < 7G6 mm <sup>2</sup> avec conducteurs auxiliaires non blindés.
Variateur à fréquence variable	SUBCAB® Flygt blindé - câble d'alimentation de moteur renforcé à 4 conducteurs blindés et deux paires torsadées de conducteurs auxiliaires. Isolation des conducteurs résistant à 90°C, autorisant des courants supérieurs. Résistance mécanique supérieure, forte résistance à l'abrasion et à l'usure. Résistance aux produits chimiques en pH 3-10 et à l'ozone, à l'huile et à la flamme. Utilisable jusqu'à une température d'eau de 70°C.

## Équipement de surveillance

- Thermocontacts s'ouvrant à 140 °C (284 °F)
- Capteur de fuite dans la chambre d'inspection (FLS10)

## Matériaux

Tableau 11: Pièces principales sauf joints mécaniques

Désignation	Matériau	ASTM	EN
Pièces coulées principales	Fonte, grise	35B	GJL-250
Boîtier de pompe	Fonte, grise	35B	GJL-250
Roue, alternative 1	Fonte, grise	35B	GJL-250
Roue, alternative 2	Fonte, Hard-Iron™	A 532 IIIA	GJN-HB555(XCR23)
Roue, alternative 3	Acier inoxydable, duplex	CD-4 MCuN	10283:2010 -1.4474
Bague d'insert, alternative 1	Fonte, grise	35B	GJL-250
Bague d'insert, alternative 2	Fonte, Hard-Iron™	A 532 IIIA	GJN-HB555(XCR23)
Chemise de refroidissement, intérieur	Acier	Consultez la norme M0326.2172.00.	
Chemise de refroidissement, alternative 1	Acier	GR65	S235JRG2
Chemise de refroidissement, alternative 2	Fabrication en acier inoxydable	AISI 316L	1.4404, 1.4432, ...
Poignée de levage	Fabrication en acier inoxydable	AISI 316L	1.4404, 1.4432, ...
Arbre	Fabrication en acier inoxydable	AISI 431	1.4057+QT800
Vis et écrous	Acier inoxydable, A4	AISI 316L, 316 et 316Ti	1.4401, 1.4404, ...
Joints toriques, alternative 1	Caoutchouc nitrile (NBR), 70° IRH	-	-
Joints toriques, alternative 2	Caoutchouc fluoré (FPM), 70° IRH	-	-
Glycol	Fluide caloporteur à base de monopropylène glycol.	-	-

Tableau 12: Joints mécaniques

Option	Joint intérieur	Joint extérieur
1	Carbure cémenté résistant à la corrosion (WCCR)/Carbure cémenté résistant à la corrosion (WCCR)	Carbure cémenté résistant à la corrosion (WCCR)/Carbure cémenté résistant à la corrosion (WCCR)
2	Carbure cémenté résistant à la corrosion (WCCR)/Carbure cémenté résistant à la corrosion (WCCR)	Carbure de silicium (RSic)/Carbure de silicium (RSic)

## Traitement de surface

Apprêt	Finition
Peint avec apprêt, voir norme interne M0700.00.0002	Couleur gris marine NCS 5804-B07G. Couche de finition bicomposante à fort extrait sec, voir norme interne M0700.00.0004 pour peinture standard et M0700.00.0008 pour peinture spéciale.

## Options

- Version pour liquide chaud (versions autres que antidéflagrante )
- Capteurs : Thermistance, FLS, Pt100, VIS 10
- Traitement de surface (Epoxy)
- Anodes en zinc
- Autres câbles

## Accessoires

Raccords de refoulement, adaptateurs, branchements de tuyaux et autres accessoires mécaniques.

Accessoires électriques tels que contrôleur de pompe, panneaux de commande, démarreur, relais de surveillance et câbles.

### 3.2 Valeur nominale et courbes de performances du moteur 3171.181/.091/.185/.095

Voici des exemples de valeurs nominales et de courbes de moteur. Pour plus d'informations, prière de contacter votre représentant local.

Le courant de démarrage triangle-étoile vaut 1/3 du courant de démarrage direct en ligne.

LT

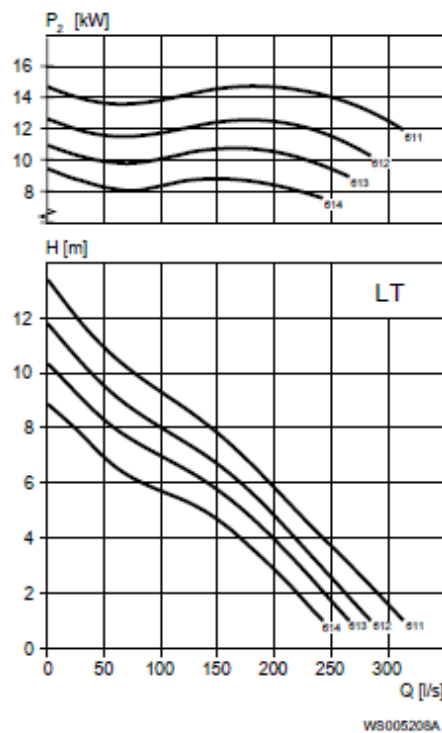


Tableau 13: 400 V, 50 Hz, triphasé

Puissance nominale, kW	Puissance nominale, ch	N° de courbe/roue	Tours par minute, tr/min	Courant nominal, A	Courant de démarrage, A	Facteur de puissance, cos $\phi$	Installation
15	20	611	965	30	167	0,84	P, S, T, Z
15	20	612	965	30	167	0,84	P, S, T, Z

